Ultrafast coincidence characteristics of entangled photons towards entangled two-photon absorption

by

Aimee K. Gunther

A thesis
presented to the University of Waterloo
in fulfillment of the
thesis requirement for the degree of
Master of Science
in
Physics - Quantum Information

Waterloo, Ontario, Canada, 2014

I hereby declare that I am the sole author of this thesis. This is a true copy of the thesis, including any required final revisions, as accepted by my examiners.

I understand that my thesis may be made electronically available to the public.

Abstract

Nonlinear optics has had extensive application into a vast array of scientific fields. One such nonlinear process, two-photon absorption (TPA), has had a wildly successful adoption into the field of biological imaging and microscopy. As far and as fast as this field is progressing, limitations stemming from the use of ultrafast lasers are starting to appear.

In this work, an alternative nonclassical light source will be motivated for the application of low photon-flux two-photon microscopy. The origin and properties of the chosen nonclassical source, spontaneous parametric downconversion (SPDC), will be discussed along with the spatial and spectral properties modelled. Nonlinear processes such as TPA and sum frequency generation (SFG) will be viewed as "ultrafast coincidence measurements" of two photons arriving at a molecule within the time window of excitation. These ultrafast coincidence measurements will be viewed in an alternative manner: in terms of the second-order coherence from a light source. This degree of second-order coherence can be subdivided into two categories arising from different combinations of correlations within and between entangled photon pairs. Of interest, the energy-time correlations within the photon pair allow for enhancements in ultrafast coincidence rates over coherent light sources. The makings of an experimental setup to demonstrate enhanced rates from ultrafast two-photon coincidences taking place in SFG in a nonlinear crystal will be discussed.

Acknowledgements

First of all, I would like to thank God, for hope anew each day. I especially would like to thank my now-husband Thomas Gunther, for loving and supporting me throughout this demanding pursuit of my dreams. To also, my friends and family, for supporting me throughout all the science-induced communication silences.

In the science community, I would like to thank my various committee members: Jim Martin, Kostadinka Bizheva, Kevin Resch and Thomas Jennewein for providing scientific feedback. I would like to thank my coworkers: Chris Pugh, John Donohue, Jonathan Lavoie, Deny Hamel, and the rest of the Quantum Photonics Laboratory for fruitful discussions, tips, skills, optical parts, and sanity. Regarding this thesis, I would like to thank Catherine Holloway, Jean-Philippe Bourgoin, Audrey Dot, and Evan Meyer-Scott, among others, for accepting my baked-goods editing bribery. I would like to thank coworkers in Vienna, Austria, Christoph Goertz and David Wartmann for the sanity, endless lab memes, and great beer during my visits.

Post docs who have greatly influenced and assisted in this work: Robert Prevedel, for collaboration and project management from afar, despite my obvious lack of email correspondence; Rolf Horn, for teaching me the art of experiment design, waveguiding, and physics in general; Piotr Kolenderski, for all-around knowledge and all that Mathematica wizardry; and Audrey Dot, for the many fruitful discussions and late night derivations.

To my supervisor, Thomas Jennewein, I'd like to thank him for giving me this great opportunity to do independent research and trusting my fledgling scientific judgement with all those Thorlabs orders. Also, Alipasha Vaziri, for teaching me how to use a lab book and pushing me to become a better scientist.

I would also like to acknowledge coffee, Bailey's, and infinite amounts of tea for fueling this degree.

Finally, I would like to thank the night janitors at RAC for being friendly, supportive, and saving me pizza.

"Never, never, never give up."

Sir Winston Churchill

Table of Contents

List of Tables

List of Figures

Chapter 1

Introduction

Nonlinear optics has had extensive application in a vast array of scientific fields. One such nonlinear process, two-photon absorption, has had a wildly successful adoption into the field of biological imaging and microscopy. As far and as fast as this field is progressing, limitations stemming from the use of ultrafast lasers are starting to appear, leaving room for improvement from alternative, nonclassical sources of light.

Rate-enhancements, from two-photon nonlinear processes, can occur from using certain types of nonclassical light, such as correlated photon pairs. This has huge potential in fields, such as two-photon fluorescence microscopy (to be discussed here); entangled two-photon absorption gates in quantum computing [1]; and the creation of nonclassical states of light in quantum optics [2].

These two-photon nonlinear processes can be viewed as ultrafast coincidence measurements. Due to limitations in the time sensitivity of current single-photon detectors, it's unfeasible to measure femtosecond coincidences using our current technology. One solution to this is to use two-photon nonlinear processes, such as two-photon absorption or sum frequency generation to generate "coincidence signals" via frequency conversion.

In this chapter, we will discuss the process of two-photon absorption and its application to microscopy. Next, principles behind ultrafast optics will be outlined, along with relevant pulse compression techniques. Finally, we will discuss alternative sources of light which mimic certain behaviours of coherent ultrashort pulses, yet allow for an increased ultrafast coincidence rate in the low photon flux regime. The current status of entangled two-photon microscopy will also be outlined.

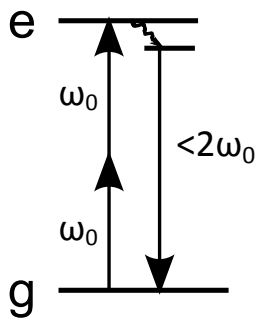

Figure 1.1: An energy diagram for TPA where, typically, the molecule relaxes to the lowest excited state before radiating a fluorescent photon. In this work, non-resonant TPA will be considered. Here, non-resonant refers to a virtual, not a real energy level between g, ground, and e, excited energy level.

1.1 Two-photon absorption

The concept of TPA was first presented in 1931 by Maria Göppert-Mayer [3]. In this process, two photons, each of half the transition energy, sum together to excite an atom from its ground to excited state. This excited atom then decays back to its initial ground state, emitting a fluorescent photon and obeying conservation of energy, as seen in Fig. 1.1.

TPA is a nonlinear process, meaning the electric field dependence is nonlinear in the medium's response [4]. Like most nonlinear processes, TPA was not experimentally demonstrated [5] until after the advent of the laser [6]. Since then, two-photon absorption has found many applications in a variety of fields, such as waveguide writing and microfabrication; upconversion lasing; optical power limiting; and microscopy and fluorescence imaging [7, and references therein]. It was the rapid adoption of TPA into the microscopy world which spurred on advancements into other TPA applications. In the subsequent section, we will briefly discuss the importance two-photon fluorescence microscopy (TPFM) over previous microscopy schemes and highlight room for nonclassical improvement.

1.1.1 Two-photon fluorescence microscopy

Two-photon absorption was first applied to laser-scanning microscopy by Denk *et al.* [8] in 1990. In laser-scanning microscopy, a laser is raster scanned across a sample and the fluorescent counts per pixel, or location, are recorded. There are many reasons why multi-photon microscopy is advantageous over one-photon absorption (1PA) imaging techniques. In 1PA, a single photon of the full transition energy is absorbed and causing a fluorescent

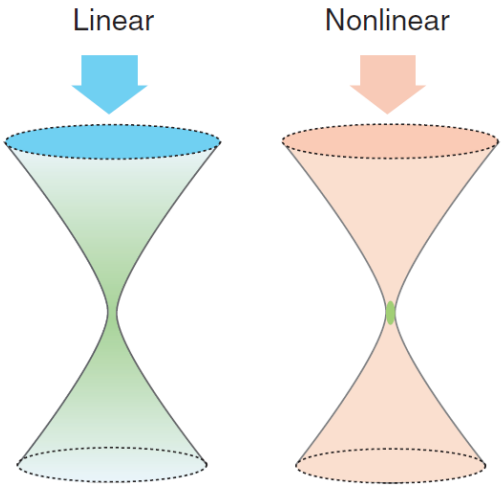

Figure 1.2: Fluorescence excitation areas for one- and two-photon absorption. Figure from [10]

photon to be emitted at a later time. In microscopy, axial image precision, or depth discrimination, can be achieved for 1PA via a clever usage of pinholes and apertures to block out-of-focus emissions (confocal microscopy) [9]. But TPA, due to its nonlinear nature, is quadratic in intensity. For this reason, only fluorophores - or fluorescent molecules - in the focal plane are excited leading all collected florescence to be counted, as seen in Fig. 1.2. This is also advantageous as it reduces the out-of-plane photodamage and photobleaching allowing samples to be imaged for longer. The longer pump wavelength used in TPFM is also advantageous due the wavelength-dependence of Rayleigh scattering, allowing much deeper imaging into the sample with still appreciable signal-to-noise [9].

TPFM was really only made practical by the development of the near-IR tunable, ultrafast, mode-locked titanium:sapphire laser [12]. The temporal localization and gigantic instantaneous peak powers available from ultrafast optics allowed for the exploration of the complex higher-order nonlinear fluorescence-emitting processes of biological systems. Two-photon absorption requires two photons, within a pulse, to be absorbed simultaneously by a fluorescent molecule. The probability of two photons arriving "simultaneously" can be increased by having a temporally very short, but intense, pulses. A practical example of two-photon absorption with a classical ultrafast laser can be seen in [13].

A typical TPFM setup is shown in Fig. 1.3. Since TPA is the near-simultaneous absorption of two photons of longer wavelength, it would seem that the shorter the pulse length, the greater the TPA rate. However, we will see in the subsequent section how pulses with a

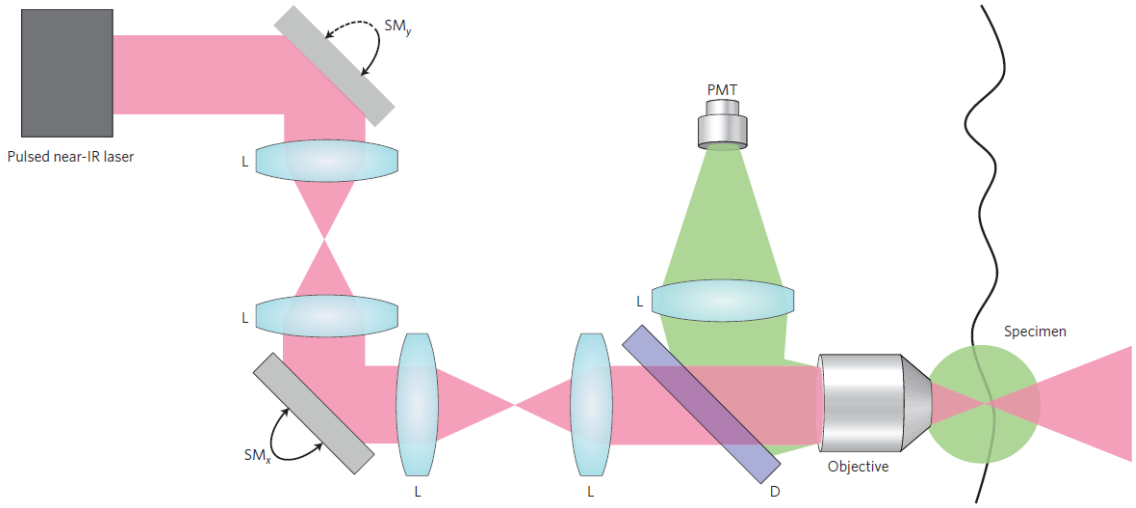

Figure 1.3: A typical two-photon fluorescence microscope for use in laser scanning microscopy. Piezo mirrors, SM_y and SM_x allow for raster scanning over the specimen. Lenses, L, allow for centred beam steering. Dichroic mirror, D, reflects the fluorescence to be focused into a PMT. Figure from [11].

short temporal pulse width (large spectral bandwidth) can lead to a frequency-dependent group delay dispersion, and thus, lowering the peak intensity in the focus. One of the main sources of this dispersion in a microscopy setup comes from the objective lenses, which are often made out of exotic and dispersive glasses. Another challenge stemming from the objective is the need to correct chromatic aberrations for the two disparate wavelengths. This is becomes challenging in microscope design as the requirement for pulses to be near-diffraction-limited in space and transform-limited in time are required for the optimization of signal per pixel [11].

TPFM, though widespread in use, is not without its drawbacks. The quadratic intensity dependence can also be damaging to sensitive samples, and for $\lambda > 900$ nm, sample heating can occur [12]. Therefore, TPFM sourced by ultrafast lasers will not be able to image deep within sensitive samples. The purpose of this work is to suggest and analyze an alternative two-photon light source: entangled photon pairs from spontaneous parametric downconversion. In order to do that, we must understand the concepts and techniques behind ultrafast optics.

1.2 Ultrafast optics

Ultrafast optics is characterized by the light-matter interactions taking place on the femtosecond (1 fs = 10^{-15} s) timescale. In this regime, fs timing precision can begin to resolve atomic and molecular processes. But, new practical challenges arise from working in this extreme regime. The time-bandwidth product, $\Delta\omega\Delta\tau \approx 1$, suggests that for the desired short time uncertainty, the resulting spectral bandwidth will be large, $\Delta\omega = \frac{1}{\Delta\tau}$. Due to the large spectral bandwidth associated with fs pulses, phases acquired in propagation through materials begin to have appreciable higher-order frequency dependence. This "dispersion" resulting from variable spectral delays result in the time-domain spread of the pulses.

The application of the complex field of ultrafast optics to biological systems came upon the invent of more "plug and play" ultrafast laser systems. The temporal localization and gigantic instantaneous peak powers available from ultrafast optics allowed for the exploration of the complex higher-order nonlinear fluorescence-emitting processes of biological systems. Two-photon absorption requires two photons, within a pulse, to be absorbed simultaneously by a fluorescent molecule. The probability of two photons arriving "simultaneously" can be increased by having a temporally very short but intense pulses. A practical example of two-photon absorption with a classical ultrafast laser can be seen in [13].

In this section, we will discuss the properties of ultrashort optical pulses needed for TPA, along with common pulse compression techniques for working with and manipulating femtosecond pulses. From here, we will also motivate an alternative light source for generating TPA – entangled photon pairs – as a solution to existing weaknesses in the current classical ultrafast TPFM.

1.2.1 Mathematical description of electromagnetic waves

Ultrafast light pulses are electromagnetic wavepackets, which can be described in both the time and frequency domain [14]. We will begin in the time domain by defining a real-valued wavepacket, free of both spatial or polarization dependence, $\mathbf{E}(x, y, z, t) = E(t)$. The complex-valued frequency representation can be found via the Fourier transform.

$$\tilde{E}(\Omega) = \frac{1}{2\pi}\mathcal{F}\{E(t)\} = \int_{-\infty}^{\infty} E(t)e^{-i\Omega t}dt = |\tilde{E}(\Omega)|e^{i\Phi(\Omega)} \tag{1.1}$$

Here, $|\tilde{E}(\Omega)|$ represents the spectral amplitude and $\Phi(\Omega)$, the spectral phase. Because $E(t)$ was initially defined as real-valued, we see that $\tilde{E}(\Omega) = \tilde{E}^*(-\Omega)$.

It is more physical to define the electromagnetic wavepacket with positive frequencies only.

$$\tilde{E}^{+}(t) = \frac{1}{2\pi}\int_{0}^{\infty} \tilde{E}(\Omega)e^{i\Omega t}d\Omega \tag{1.2}$$

$$\tilde{E}^{+}(\Omega) = |\tilde{E}(\Omega)|e^{i\Phi(\Omega)} = \begin{cases} \tilde{E}(\Omega) & \text{for} \quad \Omega \geq 0 \\ 0 & \text{for} \quad \Omega < 0 \end{cases} \tag{1.3}$$

This can be related back to the original electric fields by:

$$E(t) = \tilde{E}^{+}(t) + \tilde{E}^{-}(t) \tag{1.4}$$

$$\tilde{E}(\Omega) = \tilde{E}^{+}(\Omega) + \tilde{E}^{-}(\Omega). \tag{1.5}$$

The complex electric field is more naturally written as the product of an amplitude and phase:

$$\tilde{E}^{+}(t) = \frac{1}{2}\mathcal{E}(t)e^{i\Gamma(t)} \tag{1.6}$$

Usually we imagine an electromagnetic wavepacket centred around a central frequency, ω_0, with appreciable contributions only in a relatively small frequency interval, $\Delta\omega$, where $\Delta\omega \ll \omega_0$.

The phase in Eq. (1.6) can decomposed into $\Gamma(t) = \omega_0 t + \phi(t)$. We can minimize variations in $\phi(t)$ by defining a carrier frequency to be the central frequency, ω_0. This can be seen through the instantaneous frequency,

$$\omega(t) = \omega_0 + \frac{d}{dt}\phi(t) \tag{1.7}$$

where, for differing values of first- and second-derivatives of $\phi(t)$ we can extract information about the pulse moving in time. It is straightforward to see that for $\phi'(t) = b = \text{const}$, there will be only a constant correction to the carrier frequency. For $\phi'(t) = f(t)$, the carrier frequency will vary in time, resulting in a frequency-modulated, or linearly chirped pulse. The second-derivative in phase affects the frequency of $\omega(t)$ in time. For $\phi''(t) > 0$, $\omega(t)$ will increase along the pulse (up-chirped). Alternatively, for $\phi''(t) < 0$, $\omega(t)$ will decrease over the pulse (down-chirped). This is visualized in Fig. 1.4. As we'll see in the following sections, this phase can be altered by propagation through media and other pulse shaping techniques.

1.2.2 Pulse propagation through dispersive media

In the frequency domain, we can relate this phase from the previous section, to that acquired from passing through an optical medium of length, L,

$$\phi(\Omega) = k(\Omega)L, \tag{1.8}$$

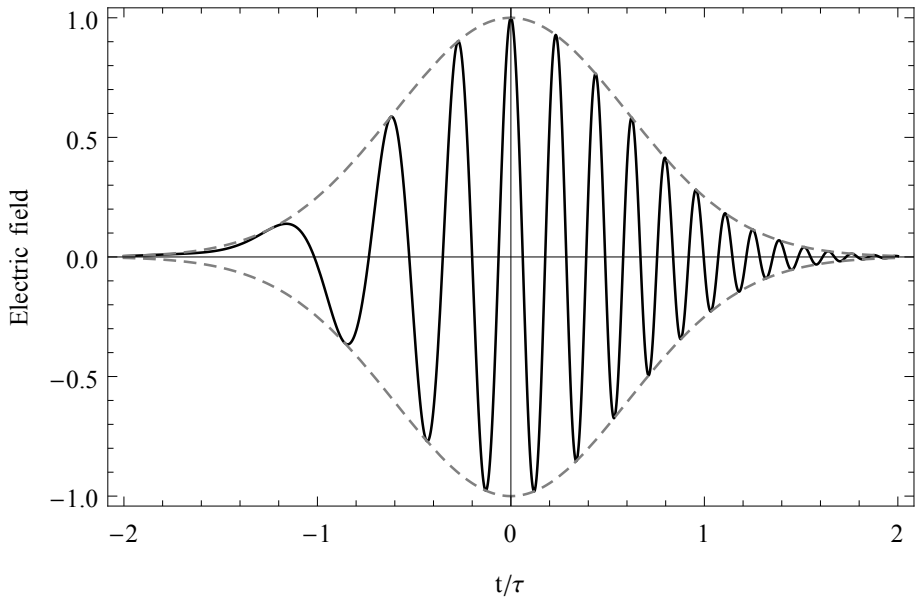

Figure 1.4: A wavepacket with a linear up chirp, as defined by a Gaussian intensity distribution, $E(t) = \exp[-2\ln 2(t/\tau_p)^2]\cos(\omega_0 t + \phi'' t^2)$, where the FWHM is $\tau_p = \frac{8\pi}{\omega_0}$, and $\phi'' = \frac{8}{\tau^2}$.

where the propagation constant, $k(\Omega) = \frac{\Omega n(\Omega)}{c}$, includes the medium's frequency-dependent refractive index, $n(\Omega)$. Since the wavepackets of interest are quite broad in frequency, we are interested in Taylor expanding out $k(\Omega)$ to second-order.

$$k(\Omega) = k(\omega_0) + \left.\frac{dk}{d\Omega}\right|_{\omega_0}(\Omega - \omega_0) + \left.\frac{d^2k}{d\Omega^2}\right|_{\omega_0}(\Omega - \omega_0)^2 + ... \tag{1.9}$$

There are a few things we can learn from Eq. (1.9). The first-order term is related to the pulse's group velocity,

$$v_g = \left(\left.\frac{dk}{d\Omega}\right|_{\omega_0}\right)^{-1}. \tag{1.10}$$

This can be understood as the speed at which the wavepacket moves. The corresponding time delay of the wavepack, when passing through a medium of length, L, is $\tau_d = \frac{L}{v_g} = \left.\frac{dk}{d\Omega}\right|_{\omega_0} L$. For large bandwidth wavepackets, the second-order term is also important. This is commonly called the group velocity dispersion (GVD):

$$\left.\frac{d^2k}{d\Omega^2}\right|_{\omega_0} = \frac{2}{c}\frac{dn}{d\Omega} + \frac{\Omega}{c}\frac{d^2n}{d\Omega^2} = \left(\frac{\lambda}{2\pi c}\right)\frac{1}{c}\left(\lambda^2\frac{d^2n}{d\lambda^2}\right). \tag{1.11}$$

This can be understood as the frequency-dependent group delay, which can be attributed to a temporally narrowband pulse spreading out in time. The GVD can be related to

the group delay dispersion (GDD) by multiplication with the medium's length. For pulses passing through "normal" material, the GVD is positive. This means that the frequency over the temporal duration of the pulse will increase leading the "redder" components to be ahead of "bluer" frequency components. Alternatively, a material is called "anomalous" if the GVD is negative. The optical glasses and materials used in this work contribute normal dispersion at the frequencies used.

Applying the concepts from above, let us show a quick example of the dispersive effects on pulse length. We will begin with a simple Gaussian pulse envelope of characteristic width, τ_G.

$$\mathcal{E}(t) = \mathcal{E}_0 e^{-\frac{t^2}{\tau_G^2}} \tag{1.12}$$

Fourier transforming Eq. (1.12) to the frequency domain, let the wavepacket now pass through an optical medium, obtaining a phase, $\phi(\Omega)$.

$$\mathcal{E}(\Omega) = \frac{\mathcal{E}_0 \tau_G}{\sqrt{2}} e^{\frac{\tau_G^2 \Omega^2}{4}} e^{-i\phi(\Omega)} \tag{1.13}$$

Expanding out the full phase under new coefficient names, $\phi(\Omega) = \sum_{n=0}^{\infty} a_n (\Omega - \omega_0)^n$, where $a_n = \frac{1}{n!} \frac{d^n}{d\Omega^n} k(\Omega) L \big|_{\omega_0}$, we see that the new frequency-domain wavepacket (truncated to second-order) is:

$$\mathcal{E}(\Omega) = \frac{\mathcal{E}_0 \tau_G}{\sqrt{2}} \exp[-i(a_0 + a_1(\Omega - \omega_0) + a_2(\Omega - \omega_0)^2)L - \frac{\tau_G^2 \Omega^2}{4}]. \tag{1.14}$$

After taking the Fourier transform back to the time domain, we see that the resulting pulse width is

$$\tau_G' = \frac{\sqrt{16 a_2^2 + \tau_G^4}}{\tau_G}, \tag{1.15}$$

which can be corrected to represent the FWHM of the intensity profile by $\tau_p = \sqrt{2 \ln 2} \tau_G$ [15].

1.3 Pulse compression

For ultrashort pulses, material dispersion can cause problems for applications requiring short and intense pulses (such as TPA). This then requires that spectrally wide-band pulses be pulse-shaped for dispersion compensation. This would allow for the result of all the frequencies within the wavepacket to arrive with minimal time uncertainty. For this reason, TPFM has come to "pre-compensate" the ultrashort pulses before entering the microscope such that by the time the pulse reaches the sample, it is at its transform-limited temporal width [16].

1.3.1 Mathematical description

An optical device which compensates for positive material GVD can be thought of as a linear element of the form [14]:

$$R(\Omega)e^{i\Psi(\Omega)}, \tag{1.16}$$

where the imparted phase, $\Psi(\Omega) = \frac{\Omega}{c}P_{OL}(\Omega)$, contains a frequency-dependent path length, $P_{OL}(\Omega)$. It is assumed that the device response, $R(\Omega)$, is constant, and thus, negligible over the spectral range of interest.

As previously discussed, the second-order (and higher) material phase affects the pulse shape and width. It is in our best interest to obtain a device which can impart a phase which behaves as

$$\frac{d^2}{d\Omega^2}\Psi(\Omega) = \frac{1}{c}\left(2\frac{dP_{OL}}{d\Omega} + \Omega\frac{d^2P_{OL}}{d\Omega^2}\right) = \frac{\lambda^2}{2\pi c^2}\frac{d^2P_{OL}}{d\lambda^2}, \tag{1.17}$$

that can be continuously tuned to produce an equal and opposite GDD. This can be viewed as a linear transfer function, $H(\Omega)$, which imparts a frequency-dependent phase [15].

To show the effect of pulse compressor, let us first expand the phase of the compressor, $\Psi(\Omega)$, to second order, to match that of the material.

$$H(\Omega) \propto e^{i(b_0+b_1(\Omega-\omega_0)+b_2(\Omega-\omega_0)^2)} \tag{1.18}$$

Picking up from Eq. (1.14), we can multiply the linear transfer function of our pulse compressor to the dispersed electromagnetic wavepacket and Fourier transform back to the time domain.

$$\mathcal{E}(t) = \mathcal{F}^{-1}\{\mathcal{E}(\Omega)H(\Omega)\} \tag{1.19}$$

This leaves us with a modified pulse width, comparable to Eq. (1.15):

$$\tau_G' = \frac{\sqrt{16(a_2+b_2)^2+\tau_G^4}}{\tau_G}, \tag{1.20}$$

where the pulse length can be modified to represent the FWHM width of the intensity profile, $|\tilde{\mathcal{E}}(t)|^2$, via $\tau_p = \sqrt{2\text{Ln}2}\tau_G$. By tuning the pulse compressor, one could minimize the pulse width when $b_2 = -a_2$.

1.3.2 Types of pulse compressors

There are multiple ways to minimize GVD, such as anomalous fibres, chirped mirrors, Gires-Tournois interferometers, diffraction gratings, and prism pairs [14, 17]. The most

common of which is based on the principal of include the use of angular dispersion. In its essence, angular dispersion occurs on pulses incident on a surface, which diffracts or refracts light as a function of frequency. For the purposes of this work, we will discuss in detail only the prism compressor which uses prisms to angularly dispersed light, though a few remarks about certain other devices will be made.

A grating compressor utilizes diffraction gratings to produce angular dispersion. It is one of the easiest pulse shaping techniques[1], however it is plagued by relatively higher loss due to four reflections off of a diffraction grating's surface. One advantage of the grating compressor comes from its ability to instill large amounts of negative GVD in a relatively small area (table space).

Before we move on, a few words on spatial light modulators (SLM). Unlike diffraction grating and prism compressors, SLMs impart a programmable frequency-dependent phase via electro-optics onto separated spectral components [15]. Angularly dispersive elements, such as gratings or prisms need to be used in conjunction with SLMs to spatially separate the different optical frequencies. SLMs can be programmed to compensate for GVD, however it's more often used for its ability to arbitrarily alter the pulse shape. We will see examples later on of SLMs being used to impart phases for higher-order interference purposes in Section 3.2.1.

1.3.3 Prism compressor

The prism compressor is the least lossy of the aforementioned pulse compression methods. The reasons for this relates back to Brewster's angle, where the transverse magnetic (or "horizontally polarized") reflection disappears for a certain $\theta_B = \tan^{-1}\left(\frac{n_f}{n_i}\right)$, for the initial and final medium's refractive index. This makes prism pulse compression possible for intracavity laser designs [17]. However, unlike grating compressors, prism compressors require long separation distances in order to compensate for relatively small amounts of GVD due to low angular dispersion. A partial solution to this problem can be solved by using more exotic, dispersive glasses. However, this leads to a detrimental increase in higher-order dispersion.

The prism compressor works as follows: a pulse passing will refract as a function of frequency after the first prism. The second prism in the compressor spatially "collimates" the separated spectral components, allowing them to propagate in a parallel, though spatially incoherent manner. In order to return to the original beam-like state, two more prisms

[1]Insightful explanations can be found in [14, 15, 17] with practical alignment instruction in [18].

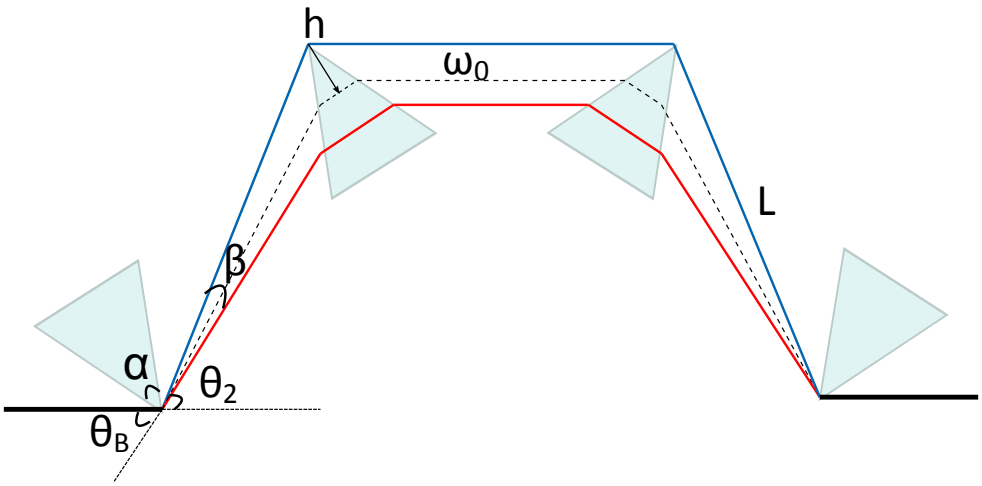

Figure 1.5: Symbolic definitions of a four prism pulse compressor, where θ_B is Brewster's angle; θ_2 is the prism exit angle; β is the angular spread; h is the beam insertion distance; ω_0 is the central frequency; and L is the prism tip-to-tip distance.

are used to do the equal and opposite spatial transformation, returning now dispersion-compensated beam back to its original mode. Since the spectrally broad pulse is passing through a dispersive medium, positive GVD will be obtained from the prism glass. However, negative contributions to the GVD from angular dispersion on the first and second interface of the first prism can be tuned to make the net GVD negative.

Fig. 1.5 shows a typical four-prism pulse compressor. This can be folded once or twice, requiring only two or one prism, respectively. The GVD imparted by this prism compressor can be described through Eq. (1.21), with further variable definitions found in Table 1.1.

$$\frac{d^2 P_{OL}}{d\lambda^2} \approx 4\left[\frac{\partial^2 n}{\partial \lambda^2} + \left(2n - \frac{1}{n^3}\right)\left(\frac{\partial n}{\partial \lambda}\right)^2\right] L \sin\beta - 8\left(\frac{\partial n}{\partial \lambda}\right)^2 L\cos\beta \tag{1.21}$$

A pulse with amassed positive GVD (red ahead of blue frequency components), will enter the prism, where the "redder" components will pass through more glass than the "bluer" components, thus will be slowed down, in addition to the path length distance. Tuning this allows for both frequencies to leave the compressor at the same time.

In this work, minimizing losses is of utmost importance due to the need for the energy-time entangled photon pair to remain intact. If one of the photons within the pair get lost, then an ultrafast coincidence can only occur if another random photon is also incident on the medium within the fs virtual state lifetime. This results in quadratic loss scaling in the fluorescent/upconverted signal. Thus, to minimize losses, this leaves the prism compressor

Table 1.1: Prism compressor variable definitions

Prism compressor	
θ_B	Brewster's angle for incident beam $= \arctan[n(\lambda)]$
α	Prism apex angle
$\theta_2(\lambda)$	Output angle of first prism $= \arcsin\left[n(\lambda)\sin\left(\alpha - \arcsin\left(\frac{\sin\theta_B}{n(\lambda)}\right)\right)\right]$
L	Apex-to-apex prism distance
h	Beam insertion distance into second prism
$\sin\beta$	Angular spread definiton $= \frac{h}{L}\frac{\cos\theta_2}{\cos(\alpha/2)}$

as the optimal method of dispersion compensation for the proposed, alternative nonclassical light source.

1.4 Motivation for a nonclassical pump source

As we saw in Section 1.1.1, TPFM has been well established with the easy-to-use ultrafast laser sources readily available. But, as it was alluded to, TPFM as we know it possesses weaknesses when imaging sensitive samples, due to its quadratic intensity dependence. It is proposed instead to use nonclassical light, which, as we'll later see, affords instead a linear intensity dependence. The nonclassical light suggested in this work is spontaneous parametric downconversion (SPDC), which will be discussed in detail in Chapter 2. An comparison between an ultrashort laser pulse and continuous wave (cw), broadband downconversion shows stark differences. However, the behavioural similarities between the two TPA light sources allow both the use of coherent control. But ultimately, as later will be discussed, its the higher-order coherence properties associated with SPDC which suggest a benefit to TPFM.

In this section, we will discuss the rate enhancement, coherent control, and relevant microscopy applications for a nonclassical light source.

1.4.1 Rate enhancement

The main motivation behind an alternative light source for TPFM comes from an enhancement in TPA rates. For a nonclassical light source, such as squeezed vacuum and SPDC[2], there is a very high correlation between photons within a generated pair. If one photon from the pair was measured in a certain time and location, the other photon has an enormously large probability of being found at a specific other time and location [19]. Since we know pairs of photons are generated together and, depending on the phasematching, travel together, it can simplistically be seen how a pair of energy-time correlated photons can be more likely to arrive and two-photon absorb than other two random photons from a classical laser pulse. These nonclassical properties lead to a rate enhancement compared to coherent laser light. In the low photon number regime, these highly correlated pair states allow for the absorption rate to scale nearly linearly, rather than quadratically in pump power in the low photon-number regime [19–21].

Multiphoton processes, such as TPA and sum-frequency generation (SFG), are sensitive to higher-order correlations in the electromagnetic field [20]. By comparing the behaviours of squeezed vacuum, coherent classical pulses, and other distributions of light under multiphoton processes, higher-order coherences can be explored.

[2]Low intensity squeezed vacuum is a superposition of even-numbered photon states (pairs). This is similar to SPDC in the single-pair emission regime.

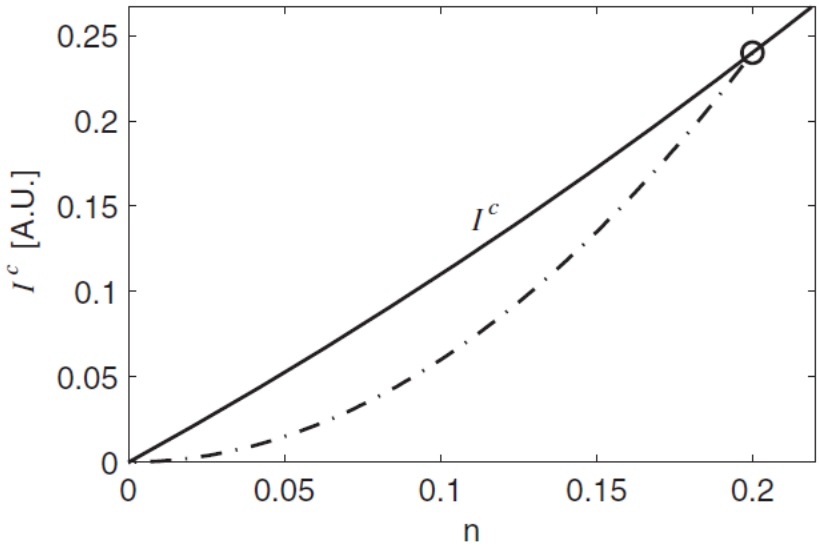

Figure 1.6: Rate enhancement from SFG and TPA via broadband downconversion. I^c represents the coherent part of the downconverted light as a function of n, the average spectral photon density. The dotted line represents the quadratic response in n to linear loss in the downconverted beam. With loss, photon pairs become separated, mimicking the quadratic intensity response of random photons from a classical laser pulse in TPA or SFG. Figure taken from Dayan [22].

The resultant signal from either TPA or SFG can come from two different sources within the downconverted beam. The "coherent" portion of signal intensity taps into the correlations within photon pair twins, which scales near linearly with photon number density [22].

$$I^c \propto n + n^2 \tag{1.22}$$

The individual photons that sum together without its twin behave as a classical laser pulse and the TPA or SFG signal reacts quadratically with photon number density [22]:

$$I^{ic} \propto n^2. \tag{1.23}$$

Since the rate of TPA and SFG is proportional to the second-order correlation function, it is then of interest to understand correlation functions and optical coherence for successful application of nonclassical light to TPFM.

Experimentally, this nonclassical linear enhancement to the rate was limited to squeezed vacuum due to limitations in nonlinear crystal technologies [21]. Coming with the advances in nonlinear optical materials (see Section 2.1.2) and detection technologies, single-photon-level nonlinear processes have become possible [23].

1.4.2 Coherent control

In order to truly replicate the TPA capabilities of coherent ultrashort pulses in broadband downconversion, its pulse shaping and phase manipulation abilities should be investigated. We can apply the techniques mentioned in Section 1.3.2 to the current discussion where "coherent control" refers mainly to arbitrary pulse phase manipulation, under which dispersion compensation still does apply.

It was shown by Meshulach and Silberberg [24] in 1998 that coherent control of femtosecond pulses can greatly affect TPA rates. Using a SLM in 4f-configuration, they sinusoidally manipulated the pulse phase as a function of wavelength. This resulted in both constructive and destructive interference in the resulting fluorescence from TPA in atomic caesium. Zheng and Wiener [25] also showed coherent control with second harmonic generation (the symmetric case of SFG) in thick nonlinear crystals, analogous to TPA [26].

One of the stark differences between broadband downconversion and coherent pulses is that downconversion is incoherent between pairs of subsequent photons [27]. But, due to the large correlation between the signal and idler (historic names of photons within the pair), the photons in the pairs can be also be coherently controlled. From this, we can see that SPDC has potential to be a very powerful alternative source of light which can be used to generate SFG or TPA at an increased (linear vs. quadratic) rate in the low photon number regime.

1.4.3 Application to two-photon microscopy

The concept of applying a SPDC photon pair source to TPFM is not new. It was proposed by Teich and Saleh [28] in 1997, and later patented by the duo in 1998 [29]. However, entangled two-photon absorption has not yet been applied to microscopy. A need does exist for new microscopy techniques for light-sensitive specimens. As microscopy pushes towards greater depth, resolution, and speed, higher classical intensities are often used, making heating in the sample from near-infrared wavelengths a problem [30]. If anything can be learned from the adoption of the tunable titanium:sapphire laser by the biological imaging community, it is that it wasn't until the engineering had been fine-tuned to the "plug-and-play" level that it was radically adopted. Given the inherent vulnerability and sensitivity of quantum states of light to noise and decoherence, there is likely still a long time until a quantum optics "laser jock" [9] is no longer necessary for use of an entangled two-photon microscope. This all being said, with ever-increasing technologies, the entangled two-photon microscope is an important goal and great future application for current work in

entanglement-enhanced coincidence detection.

This thesis will study the theoretical background behind the chosen source of nonclassical light, SPDC. A quantum mechanical derivation of SPDC will be shown in Chapter 2. Further steps will also be taken to demonstrate spatial modelling in a uniaxial crystal. In order to understand how an entangled photon pair source could be beneficial, we will study first- and second-order coherence in Chapter 3, highlighting experimental examples of such. Finally, an experiment to demonstrate these entanglement-enhanced ultrafast coincidences will be proposed in Chapter 4.

Chapter 2

A source for entangled photon pairs

Entangled photons can be created in a variety of methods. Atomic sources made from cascading atomic transitions were the first successful sources of polarization-entangled photon pairs [31, 32]. Recently, there has been interest in semiconductors for use as single-photon sources [33, 34]. Polarization-entangled photon pairs from semiconductor quantum dots can also be created via cascaded two-photon emission [35]. Spontaneous four-wave mixing can produce entangled photon pairs in $\chi^{(3)}$ nonlinear material [36, 37].

The most common source of entangled photon pairs – and the main subject of this work – comes from the process of spontaneous parametric downconversion (SPDC). This chapter will discuss the different properties of SPDC with respect to our goal: to design a source capable of entanglement-assisted two-photon absorption. First, we will discuss the quantum mechanical theory behind SPDC, followed by the theoretical modelling of SPDC for the experiment proposed, and finally, a comparison between experimental and theoretical spatial and spectral profiles.

2.1 Spontaneous parametric downconversion

Spontaneous parametric downconversion occurs when one pump photon spontaneously splits into two daughter photons within a second-order nonlinear dielectric material. This process occurs when the phasematching conditions of the crystal are satisfied. Due to the laws of physics, frequency conversion must conserve both energy and momentum:

$$\omega_p = \omega_s + \omega_i \tag{2.1}$$

$$\mathbf{k}_p = \mathbf{k}_s + \mathbf{k}_i, \tag{2.2}$$

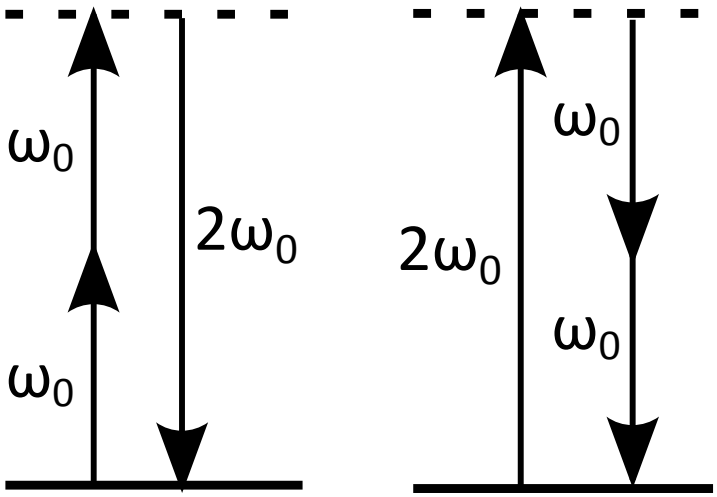

(a) Sum frequency generation (SFG)

(b) Spontaneous parametric downconversion (SPDC)

Figure 2.1: Second-order nonlinear frequency conversion within a nonlinear crystal. The excited state is virtual, designated by a dashed line. These processes of SFG (or, in the special case shown here, second-harmonic generation) and SPDC are parametric due to energy conversion.

where bold font in this work represents vector quantities.

The reverse process is sum frequency generation (SFG), which occurs when two photons merge together in a nonlinear material to produce one photon of twice the energy. In SFG, in the special case when two photons incident on the nonlinear crystal are equal, as shown in Fig. 2.1a, then the process is referred to as second harmonic generation (SHG). This process can be explained classically, unlike SPDC which is a purely quantum process, due to the initial signal and idler fields at the start.

Photon pairs created from SPDC are said to be entangled, or quantumly-correlated, with each other. A photon pair may be entangled in numerous degrees of freedom, such as: polarization [38, 39], time-bin [40], spatial mode [41], orbital angular momentum [42], and energy-time [43, 44]. A hyperentangled photon pair can exhibit multiple entangled modes at once [45].

With the variability of parameters available for SPDC source engineering, an optimal source for ETPA can be developed. In this section, the wavefunction of SPDC will be derived from the nonlinear interaction Hamiltonian. Spectral engineering techniques, such as quasi-phasematching, will be included in development of the SPDC wavefunction to motivate an energy-time entangled source for ETPA.

2.1.1 Nonlinear interaction Hamiltonian

SPDC is a process which occurs within nonlinear dielectric media. It wasn't until the advent of the laser [6] that the medium's nonlinear susceptibility became more readily accessible via strong electric field intensities. A common way to express a medium's nonlinear response is through the polarization of the dipoles within the medium. In the simplest case, for isotropic, dispersionless material, this is

$$P_i = \chi_{ij}^{(1)} E_j + \chi_{ijk}^{(2)} E_j E_k + \dots, \tag{2.3}$$

where E_j is the electric field within the medium, $\chi^{(m)}$ is a tensor of rank m, and i, j, k distinguish the different fields [4].

Though there are many processes stemming from $\chi^{(2)}$ nonlinearity, the one of primary interest in this work is that of SPDC. In this process, a classical, strong pump parametrically "down-converts" to two photons of energies summing to the pump energy. In this derivation, the pump will be described as a monochromatic plane wave,

$$\hat{E}_p = E_0(\mathbf{k_{p,\perp}}) e^{-i(\mathbf{k_p}\cdot\mathbf{r}-\omega_p t)} \hat{\varepsilon}_p \tag{2.4}$$

where E_0 is the pump amplitude, $\mathbf{k_{p,\perp}}$ is the perpendicular k-vector components of the pump, ω_p is the optical pump frequency, and $\hat{\varepsilon}_p$ is the unit vector in the pump direction, aligned along the z-axis. The signal and idler electric fields need to be modelled nonclassically on the single-photon level [46]. Single-mode fields will be considered:

$$\hat{E}_j^{(-)} = -i \int dk_z \sqrt{\frac{\hbar k_{j,z} c^2}{4\pi\epsilon_0 S_Q n^2(k_{j,z})}} \hat{\varepsilon}_j \hat{a}^\dagger(\omega_j) e^{-i(k_{j,z}z-\omega_j t)}. \tag{2.5}$$

where j represents the signal or idler, $\hat{a}^\dagger(\omega_j)$ is the creation operator, and S_Q is the quantization area. Similarly, it's negative frequency component hermitian conjugate is:

$$\hat{E}_j^{(+)} = +i \int dk_{j,z} \sqrt{\frac{\hbar k_{j,z} c^2}{4\pi\epsilon_0 S n^2(k_{j,z})}} \hat{\varepsilon}_j \hat{a}(\omega_j) e^{i(k_{j,z}z-\omega_j t)}. \tag{2.6}$$

As previously alluded to, SPDC is based on a three-wave mixing process. The interaction Hamiltonian inside the medium can be separated into linear and nonlinear components.

$$\mathcal{H}_I = \mathcal{H}_I^L + \mathcal{H}_I^{NL} \tag{2.7}$$

The interaction Hamiltonian describing the nonlinear part is [47]:

$$\mathcal{H}_I^{NL} = -\epsilon_0 \int_V \chi^{(2)} dV_i \left(\hat{E}_i^{(+)} \hat{E}_j^{(-)} \hat{E}_k^{(-)} + \hat{E}_i^{(-)} \hat{E}_j^{(+)} \hat{E}_k^{(+)} \right), \tag{2.8}$$

where $V = L_x L_y L_z$ is the volume of the nonlinear medium, and ϵ_0 is the vacuum permittivity.

Using first-order perturbation theory, we can act the time-independent Hamiltonian onto the initial signal and idler vacuum states,

$$\begin{aligned}|\psi\rangle &= e^{-i/\hbar \int_0^t \mathcal{H}_I^{NI}(t')dt'} |0\rangle_s |0\rangle_i \\ &= |0\rangle_s |0\rangle_i + \frac{i}{\hbar}\chi^{(2)}\frac{\epsilon_0}{2}\int_0^t dt' \int_V dV \left(E_i^{(+)}E_j^{(-)}E_k^{(-)} + E_i^{(-)}E_j^{(+)}E_k^{(+)}\right)|0\rangle_s|0\rangle_i + ... \end{aligned} \tag{2.9}$$

where $\hbar$ is Planck's constant, and $|0\rangle_s|0\rangle_i$ is the initial vacuum state. We see that only the second term term is interesting for pair generation. It now evident that the $E_i^{(-)}E_j^{(+)}E_k^{(+)}$ term of the Hamiltonian will not contribute to the final state due to the annihilation operators of Eq. (2.5) acting the initial vacuum state of the signal and idler modes. Extending this interaction to higher orders, the SPDC state is

$$|\psi\rangle = |\psi^{(0)}\rangle + |\psi^{(2)}\rangle + |\psi^{(4)}\rangle + ... \tag{2.10}$$

where, in general, the biphoton state of interest is $|\psi^{(2)}\rangle$. The SPDC process of interest in this work is Type 0, where all the fields are polarized along the extraordinary axis of the nonlinear crystal. Refer to Section 2.2.1 for further discussion on crystal structures. For this reason, $\hat{\varepsilon}_p = \hat{\varepsilon}_s = \hat{\varepsilon}_i$, and will be dropped from subsequent discussion.

Inserting the appropriate electric fields (Eq. (2.4), Eq. (2.5)) into the second-order term of Eq. (2.9) yields the following:

$$\begin{aligned}|\psi^{(2)}\rangle =& \frac{i}{2}\chi^{(2)}\int_t dt' \int_V dV \left[-i\int dk_{i,z}\sqrt{\frac{\hbar k_{i,z}c^2}{4\pi S_Q n^2(k_{i,z})}}\hat{\varepsilon}_j \hat{a}^\dagger(\omega_i)e^{-i(k_{i,z}z-\omega_j t)}\right]\times \\ &\left[-i\int dk_{s,z}\sqrt{\frac{\hbar k_{s,z}c^2}{4\pi S_Q n^2(k_{s,z})}}\hat{\varepsilon}_j \hat{a}^\dagger(\omega_s)e^{-i(k_z z-\omega_j t)}\right]\times\left[E_0(\mathbf{k}_{\mathbf{p},\perp})e^{i[(\mathbf{k}_{\mathbf{p},\perp}+k_{p,z})\cdot\mathbf{r}-\omega_p t]}\right]|0\rangle_s|0\rangle_i.\end{aligned} \tag{2.11}$$

We can define the phasemismatch, $\Delta k_z = k_{p,z} - k_{s,z} - k_{i,z}$ from the combined exponentials.

The spatial integration can be done using the following trick:

$$\begin{aligned}\int_0^{L_z} dz e^{-i\Delta k_z z} &= -\frac{i}{\Delta k_z}(1 - e^{-i\Delta k_z L_z}) \\ &= L_z e^{-i\frac{\Delta k_z L_z}{2}}\frac{\sin(\frac{\Delta k_z L_z}{2})}{\frac{\Delta k_z L_z}{2}} \\ &= L_z e^{-i\frac{\Delta k_z L_z}{2}}\mathrm{sinc}(\frac{\Delta k_z L_z}{2}).\end{aligned} \tag{2.12}$$

In the limit that the beam area is large enough such that the diffraction effects can be ignored [46], the perpendicular spatial sinc functions can be approximated by delta functions.

$$|\psi^{(2)}\rangle \approx \frac{ic}{2}\chi^{(2)}E_p(\mathbf{k_{p,\perp}})\int_t dt'\int dk_{s,z}\int dk_{i,z}L_z e^{\frac{-i}{2}(\Delta k_z L_z)}\sqrt{\frac{k_{i,z}c^2}{n^2(k_{i,z})}\frac{k_{s,z}c^2}{n^2(k_{s,z})}}$$
$$\text{sinc}(\frac{\Delta k_z L_z}{2})e^{-i(\omega_p-\omega_s-\omega_i)t'}\hat{a}^\dagger(\omega_s)\hat{a}^\dagger(\omega_i)|0\rangle_s|0\rangle_i \tag{2.13}$$

Since the integration time of the fields inside the medium is much longer than $\frac{1}{\omega}$, the temporal integration can be replaced by $\delta(\omega_p-\omega_s-\omega_i)$, and it's accompanying oscillatory factor disregarded [48].

We can convert from wavevector to frequency by $dk \simeq n(\omega)d\omega/c$ so that our biphoton wavefunction now looks like:

$$|\psi^{(2)}\rangle \simeq \frac{i}{2c}\chi^{(2)}E_p L_z(\mathbf{k_{p,\perp}})L_z \tag{2.14}$$
$$\int_{\omega_s}d\omega_s\int_{\omega_i}d\omega_i\sqrt{\frac{\omega_s}{n(\omega_s)}\frac{\omega_i}{n(\omega_i)}}\text{sinc}(\frac{\Delta k_z L_z}{2})\delta(\omega_p-\omega_s-\omega_i)\hat{a}^\dagger(\omega_s)\hat{a}^\dagger(\omega_i)|0\rangle_s|0\rangle_i$$

where the frequencies under the square root are assumed to be relatively narrowband, and thus we can ignore the square root inside the summation. Collecting the prefactors into a constant, C, the biphoton state is now:

$$|\psi^{(2)}\rangle \simeq CE_p(\mathbf{k_{p,\perp}})L_z\int_{\omega_s}d\omega_s\int_{\omega_i}d\omega_i\text{sinc}(\frac{\Delta k_z L_z}{2})\delta(\omega_p-\omega_s-\omega_i)|1,\omega_s\rangle_s|1,\omega_i\rangle_i \tag{2.15}$$

The SPDC biphoton wavefunction has inherent energy correlations between created signal and idler photons. The delta function enforces energy conservation between the fixed pump frequency and the variable daughter photon frequencies.

2.1.2 Quasi-phasematching

The downconversion bandwidth limitations are determined by the frequency dispersion and birefringence[1] from the wavevector mismatch, $\Delta k_j(\omega)$. By careful choices in crystal cut, angle, and temperature, one can use birefringence to achieve phasematching conditions in some nonlinear material [49]. However, this is not a universal solution. Some materials, such as GaAs, have no birefringence, due to crystal structure. Or, in the short wavelength regime, the refractive index "blows up" disproportionate to that of the birefringence [50].

[1] The difference between the phase velocities of orthogonally polarized waves

When the parametric process hinges on the three waves having the same polarization, as is the case in this work, this technique of birefringence cannot be used to compensate for phase-mismatch-inducing dispersion [4].

The idea for quasi-phasematching occured very early on by Armstrong *et al.* [51], who suggested rotating thin slices of the nonlinear optical medium by 180°. This approach can be difficult to fabricate, depending on the thickness of the slices. The method currently used today is called *periodic poling* [52], where one optical axis is varied periodically over the length of the material. Further reading on the topic can be found in [4, 15, 49, 53].

Within the medium, the interaction efficiency decreases after a certain coherence length, $L_{\text{coh}} = \frac{\pi}{\Delta k_z}$, due to the position-dependent phases $\mathbf{\Delta k} \cdot \mathbf{r}$. By periodically switching the optical axis, the nonlinear interaction can grow monotonically over the length of the crystal [49].

The optimal poling period, $\Lambda = 2L_{\text{coh}}$, is twice the coherence length, L_{coh}, and is dependent on the phasemismatch and the corresponding dispersion properties of the medium. This leads to the pump seeing the nonlinear susceptibility[2] inside the crystal as

$$d(z) = d_{\text{eff}} \text{sign}[\cos(\frac{2\pi z}{\Lambda})]. \tag{2.16}$$

We can rewrite this as a Fourier series,

$$d(z) = d_{\text{eff}} \sum_{m=-\infty}^{\infty} G_m \exp[ik_m z], \tag{2.17}$$

where $k_m = \frac{2\pi m}{\Lambda}$, and $G_m = \left(\frac{2}{m\pi}\right) \sin(\frac{m\pi}{2})$. Making the assumption that one particular Fourier component will provide the dominant coupling, it's straightforward to see that the $m = 1$ will yield the largest G_m contribution. This brings the phase mismatch to become

$$\Delta k_z' \equiv \Delta k_z - \frac{2\pi}{\Lambda} \tag{2.18}$$

where $\Delta k_z = k_p(\omega_p) - k_s(\omega_s) - k_i(\omega_p - \omega_s)$.

Inserting Eq. (2.18) into Eq. (2.15), we obtain the new biphoton wavefunction, written with the final angular frequency integration.

$$|\psi^{(2)}\rangle \approx C \int_{\omega_s} \int_{\omega_i} d\omega_s d\omega_i \text{sinc}\left[\Delta k_z'(\omega_s, \omega_i)\frac{L_z}{2}\right] \delta(\omega_p - \omega_s - \omega_i)|1, \omega_s\rangle_s |1, \omega_i\rangle_i \tag{2.19}$$

[2]Where the nonlinear susceptibility is written in Kleinman notation, $d_{ijk} = \frac{1}{2}\chi^{(2)}_{ijk}$, where $j = k$ and can be contracted to $jk \to l$. Most dielectric crystals abide with the Kleinman symmetry condition, where the frequencies of interest are far smaller than the material's resonant frequency. Further discussion on d_{eff} and crystal symmetries can be found in [4]

2.2 Modelling of SPDC for periodically-poled lithium niobate

For TPA, it is optimal to have a SPDC source which produces daughter photons with the same polarization. For this reason, we obtained a specific sample of periodically-poled lithium niobate (PPLN) exhibiting the polarization requirements through the process of Type 0 SPDC.

We will begin by approximating a joint spectral density function capable of tractable symbolic manipulation in *Mathematica*, or the like. In this thesis, uniaxial crystal are of interest. Likewise a variety of noncollinear SPDC processes using this crystal structure will be discussed.

In this work, experimental findings encouraged an investigation into the spatial characteristics of Type 0 SPDC in PPLN. This process is modelled using the discussed techniques and compared to experimental spatial distributions.

2.2.1 Mathematical Wavefunction

While the wavefunction in Eq. (2.19) seems fairly straightforward, however it's mathematically challenging to integrate complicated sinc functions due to the singularity at $x = 0$. In order to tractably model SPDC, a few approximations are necessary.

The amplitude of the biphoton wavefunction is the product of the phasematching term, $\text{sinc}\left[\Delta k_z'(\omega_s, \omega_i)\frac{L_z}{2}\right]$, and the spatiotemporal pump contributions [54, 55].

$$\begin{aligned}|\psi^{(2)}\rangle &\simeq CE_p(\mathbf{k}_{\mathbf{p},\perp})\int_{\omega_s} d\omega_s \int_{\omega_i} d\omega_i \text{sinc}(\frac{\Delta k_z L_z}{2})\delta(\omega_p - \omega_s - \omega_i)|1,\omega_s\rangle_s|1,\omega_i\rangle_i \\ &\simeq C\int_{\omega_s}\int_{\omega_i} d\omega_s d\omega_i \Psi(\omega_s,\omega_i)E_p(\mathbf{k}_{\mathbf{p}\perp},\omega_s,\omega_i)|1,\omega_s\rangle_s|1,\omega_i\rangle_i \end{aligned} \tag{2.20}$$

where the transverse pump profile is approximated by a Gaussian, parameterized as:

$$\begin{aligned}E_p(\mathbf{k}_{\mathbf{p}\perp},\omega_s,\omega_i) &= E_p^{\text{spat}}(\mathbf{k}_{\mathbf{p}\perp})E_p^{\text{temp}}(\omega_s,\omega_i) \\ &= \left(e^{-\frac{1}{2}\mathbf{k}_{\mathbf{p},\perp}{}^2 w_p^2}\right)\delta(\omega_p - \omega_s - \omega_i),\end{aligned} \tag{2.21}$$

where the cw nature of the pump beam more than adequately allows for the delta function approximation.

The joint spectral function, or phasematching term can also be approximated by a Gaussian, as seen in Fig. 2.2, for small deviations around $x = 0$.

$$\Psi(\omega_s,\omega_i) = e^{-\frac{i}{5}\Delta k_z(\mathbf{k_s},\perp,\mathbf{k_i},\perp,\omega_s,\omega_i)z} \tag{2.22}$$

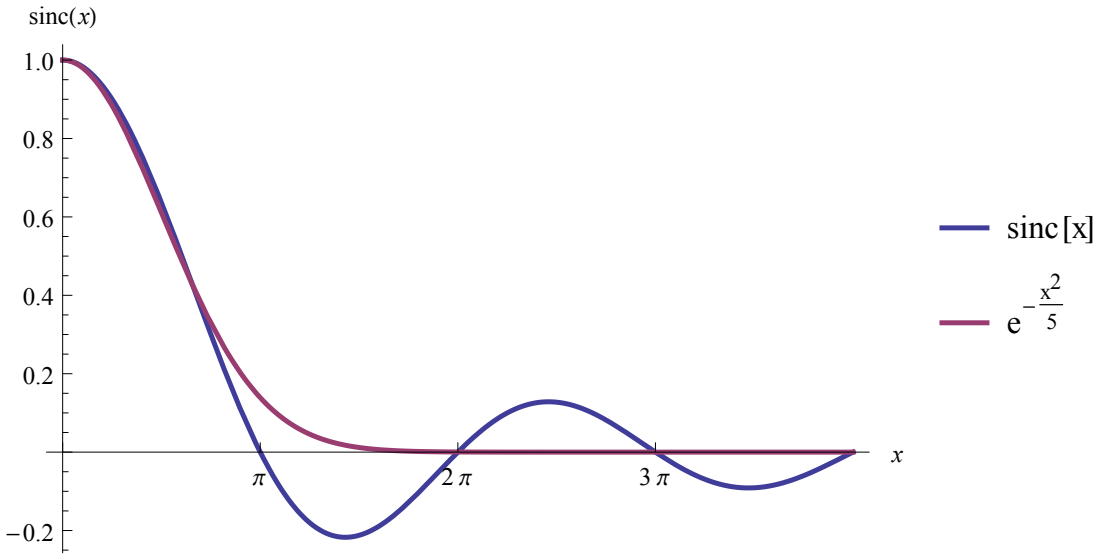

Figure 2.2: Gaussian approximation of a sinc function.

By enacting energy conservation, $\omega_i = \omega_p - \omega_s$, where the pump frequency is fixed, the above definition can be simplified to:

$$\Psi(\omega_s) = e^{-\frac{i}{5}\Delta k_z(\mathbf{k_s},_\perp,\mathbf{k_i},_\perp,\omega_s)z}. \tag{2.23}$$

We will see in the next section how crystal-specific properties can limit the phasematching of three-wave mixing.

Modelling nonlinear crystal structures

Interesting properties and limitations to SPDC arise out of the families of nonlinear crystals technically developed for periodic poling. The families of lithium niobate ($LiNbO_3$, LN) and lithium tantalate ($LiTaO_3$, LT) have been explored for frequency conversion waveguide technologies [49]. They both have large d_{33} nonlinear coefficients at 28 pm/V and 16 pm/V for LN and LT, respectively. The accessible nonlinearity in LN is the largest among commonly used ferroelectrics [49]. The crystal offers transparency from under 400 nm to the mid-IR (4 μm) offering a wide range of frequency conversion from 460 nm to 2.8 μm. These crystals, however, are susceptible to photorefractive damage (refractive index variance, distorting the beam) and absorption changes (photochromic effects) [49]. Recent advances in periodic poling and doping with MgO has greatly improved crystal performance.

The other main family of periodically-poled nonlinear crystals is the potassium titanyl phosphate ($KTiOPO_4$, KTP) family. In comparison to the LN family, the d_{33} coefficient

is smaller (17 pm/V), however KTP has a much greater resistance to photorefractive and surface damage. Frequency conversion ranging from 359 nm to 2.74 μm have been generated from PPKTP devices [49].

When modelling any polarization-dependent process through a nonlinear crystal, the symmetry of the crystal structure must be taken into account in order to understand the limitations of the phasematching. Reactions to the linear susceptibility separate different crystal lattice structures [4]. Cubic and isotropic structures yield an equal, diagonal $\chi^{(1)}$ for an isotropic behaviour within the crystal. Everything else is anisotropic. Other crystal structures are characterized as:

- Tetragonal, trigonal, hexagonal $\rightarrow$ uniaxial
- Triclinic, monoclinic, orthorhombic $\rightarrow$ biaxial

A coordinate system can always be chosen such that the off-diagonal terms in the $\chi^{(2)}$ tensor are zero. These axes are called the principal axes. With respect to the plane made by the optic axis and the propagation vector, $\mathbf{k}$, the perpendicular polarization is called *ordinary, o* and the parallel polarization to the plane is *extraordinary, e* [4].

Uniaxial crystals are symmetric about one axis, often called the optic axis of the crystal. The principal axes for uniaxial crystals are then defined as $n_1 = n_2 = n_o$, $n_3 = n_e$. Uniaxial crystals can further be subdivided into two categories: *negative* uniaxial ($n_e < n_o$) and *positive* uniaxial ($n_e > n_o$). Biaxial crystals, as expected, have all different refractive indices as principal axes: $n_1 < n_2 < n_3$. Crystal designations relevant to this work: LN is negative uniaxial, and KTP is positive biaxial.

The polarization dependence of SPDC allows for three different types of phasematching interactions: Type 0, Type 1, and Type 2. Type 0 phasematching is where the polarizations of the pump, signal, and idler are all along the extraordinary axis, designated as "eee". These beams all travel at the same group velocity and experience the same dispersion. Type 1 interactions are generally "eoo" or "oee" with the same polarization for signal and idler, and Type 2, "eoe" or "oeo" with mutually orthogonal signal and idler.

Drawing on the motivation from the previous chapter, TPA requires the signal and idler to have the same polarization; this leaves us with Type 0 or Type 1. Given that we want the most efficient crystal possible (since the downconversion acts as the pump for TPA), PPLN is a good choice. Subsequent crystal analysis will be modelled for the negative uniaxial nature of PPLN.

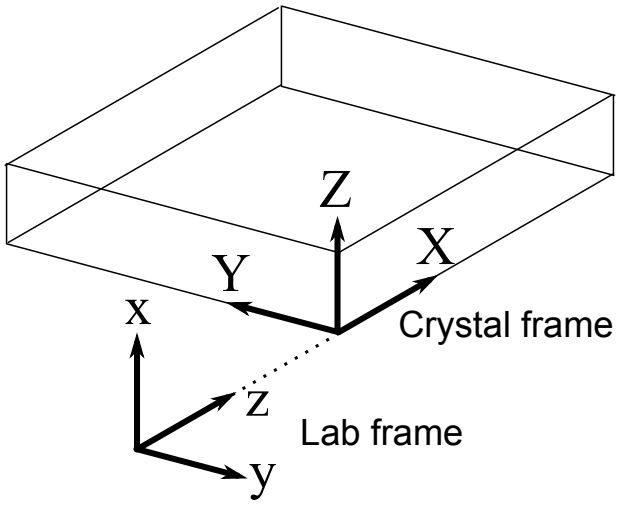

Figure 2.3: Crystal and lab coordinate systems used in this thesis.

The dispersion relation for a uniaxial crystal yields different solutions for k_o than for k_e [15]. The PPLN crystal of interest is "Z" cut, meaning that the optic axis (which is periodically flipped) is facing upwards. For reasons of simplicity and tradition, let us define a different lab coordinate system, as demonstrated in Fig. 2.3. Let the uppercase labels define the crystal coordinate system and the lowercase labels be for the lab frame:

$$\mathbf{k_z} = \mathbf{k_X} \tag{2.24}$$

$$\mathbf{k_y} = -\mathbf{k_Y} \tag{2.25}$$

$$\mathbf{k_x} = \mathbf{k_Z}. \tag{2.26}$$

Given the negative uniaxial nature of the crystal, we need to obtain a complete description[3] of k_e for the phase mismatch in Eq. (2.18) [56].

$$\begin{aligned} \frac{k_X^2 + k_Y^2}{n_e^2} + \frac{k_Z^2}{n_o^2} &= k_0^2 \\ \frac{k_z^2 + (-k_y)^2}{n_e^2} + \frac{k_x^2}{n_o^2} &= k_0^2 \end{aligned} \tag{2.27}$$

Relative to the propagation direction, we can separate this into the parallel (k_z) and

[3]For an interesting three-dimensional visualization of Eq. (2.27), see Section A.1 of Appendix A

perpendicular (k_x, k_y) components,

$$\begin{aligned} k_x &= n_e\sqrt{k_0^2 - \frac{k_z^2}{n_o^2} - \frac{k_y^2}{n_e^2}} \\ k_y &= n_e\sqrt{k_0^2 - \frac{k_z^2}{n_o^2} - \frac{k_x^2}{n_e^2}} \\ k_z &= n_o\sqrt{k_0^2 - \frac{k_x^2}{n_e^2} - \frac{k_y^2}{n_e^2}} \end{aligned} \tag{2.28}$$

Finally, we have the tools to accurately model noncollinear emission of SPDC. The phase mismatch is:

$$\begin{aligned} \Delta k_z =& n_e(2\omega_0)\sqrt{\frac{(2\omega_0)^2}{c^2} - \frac{(k_{s,x}+k_{i,x})^2}{n_o^2(2\omega_0)} - \frac{(k_{s,y}+k_{i,y})^2}{n_e^2(2\omega_0)}} \\ &- n_e(\omega_s)\sqrt{\frac{(\omega_s)^2}{c^2} - \frac{k_{s,x}^2}{n_o^2(\omega_s)} - \frac{k_{s,y}^2}{n_e^2(\omega_s)}} \\ &- n_e(2\omega_0-\omega_s)\sqrt{\frac{(2\omega_0-\omega_s)^2}{c^2} - \frac{k_{i,x}^2}{n_o^2(2\omega_0-\omega_s)} - \frac{k_{i,y}^2}{n_e^2(2\omega_0-\omega_s)}} - \frac{2\pi}{\Lambda}, \end{aligned} \tag{2.29}$$

where energy and momentum conservation has been applied to the following substitutions: $k_{p,x} = k_{s,x} + k_{i,x}$, $k_{p,y} = k_{s,y} + k_{i,y}$, and $2\omega_0 = \omega_s + \omega_i$.

2.2.2 Noncollinear broadband emission

In an attempt to explain the spatial behaviour of the Type 0 downconversion observed, we modelled the spatial emission of the PPLN source. Since PPLN is a negative uniaxial crystal, the phase mismatch from Eq. (2.29) was used. In order to make Eq. (2.28) tractable for symbolic integration, Δk_z needs to be Taylor-expanded to second-order in ω_s and first-order in $k_{s,x}$, $k_{i,x}$, $k_{s,y}$, and $k_{i,y}$.

$$\begin{aligned} \Delta k_{z,\text{approx}} =& 2\frac{\omega_0}{c}(n_e(2\omega_0) - n_e(\omega_0)) - \frac{\omega_0 c k_{i,x} k_{s,x} n_e(2\omega_0)}{2\omega_0^2 n_o(2\omega_0)^2} \\ &- \frac{k_{i,y}k_{s,y}\frac{\omega_0}{c}(c^4 k_{i,x}k_{s,x} + 4c^2\omega_0^2 n_o(2\omega_0)^2)}{8\omega_0^4 n_e(2\omega_0) n_o(2\omega_0)^2} - (\omega_s-\omega_0)^2\left[\frac{2\frac{\omega_0}{c}n_e'(\omega_0)}{\omega_0} - \frac{\omega_0}{c}n_e''(\omega_0)\right] - \frac{2\pi}{\Lambda} \end{aligned} \tag{2.30}$$

This $\Delta k_{z,\text{approx}}$ is inserted into Eq. (2.23) and analytically integrated over all ω_s, $k_{i,x}$, and $k_{i,y}$. We then look at spatial emission information along the x axis in the signal photon

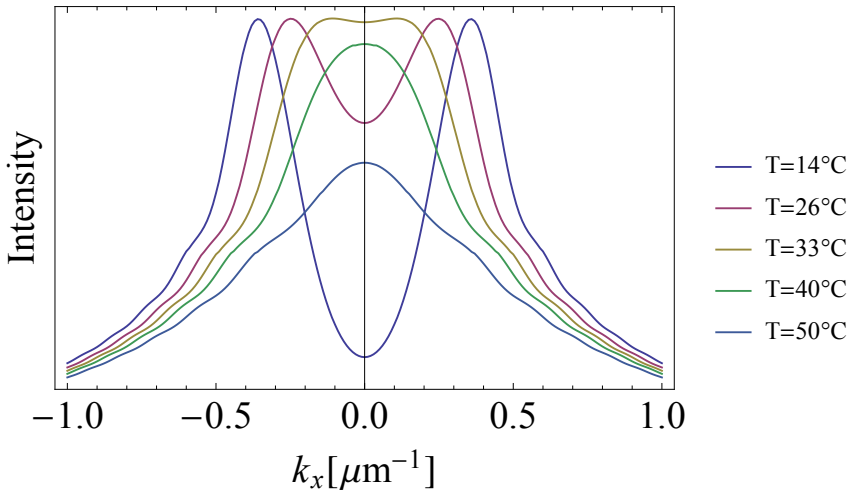

Figure 2.4: Temperature variations on spatial SPDC emission without bandpass filtering taken at a fixed beam waist of $w_p = 45$ μm.

after numerically integrating over the crystal length, as in Eq. (2.12). The results for these calculations, with and without a spectral bandpass filter, are discussed in the following sections.

Spatial emission of Type 0 SPDC

The spatial emission results over all wavelengths are seen in Fig. 2.4. The perpendicular wavevector can be related to an emission half-angle, α_{PPLN}, in the crystal by,

$$k_x = \frac{2\pi}{\lambda} \sin \alpha_{\mathrm{PPLN}}. \tag{2.31}$$

The observed half-angle in air can be found via Snell's law:

$$n_{\mathrm{PPLN}} \sin \alpha_{\mathrm{PPLN}} = n_{\mathrm{air}} \sin \alpha_{\mathrm{air}}. \tag{2.32}$$

The half-angle, taken at the FWHM of the $T = 26°\mathrm{C}$ emission curve, is 2.3°. From the curves in Fig. 2.4, it is evident that the emission is highly noncollinear for low temperatures beneath the degenerate temperature ($T = 26°\mathrm{C}$, yellow curve). For higher temperatures, the overall shape of the emission is predominantly collinear, but has less intensity than that of degenerate phasematching.

The relative intensities of the spatial emission spectrum are highly dependent on the tightness of the beam waist within the crystal, as seen in Fig 2.5. Given the experimental setup (discussed in Section 2.2.3), the relevant beam waist is $w_p = 45$ μm. For a larger

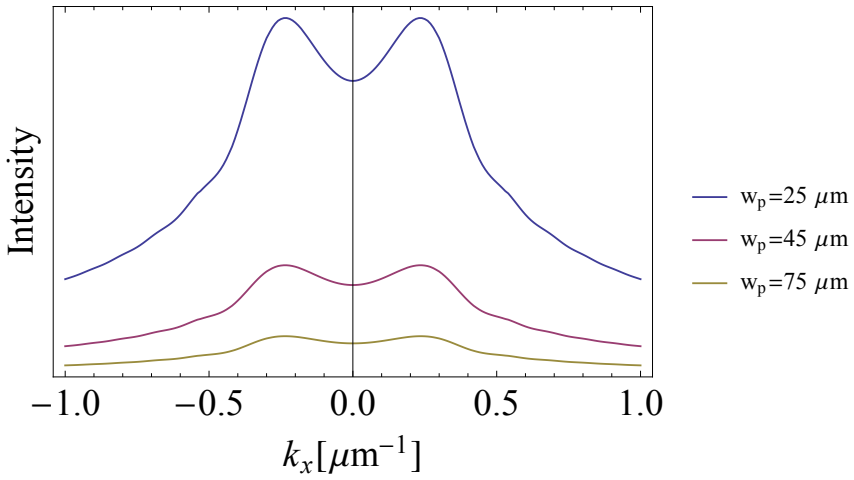

Figure 2.5: Beam size variations on spatial SPDC emission without bandpass filtering taken at fixed $T = 26°\text{C}$.

beam waist, there is a lower overall intensity. Likewise, for a smaller beam waist, a much larger SPDC emission. This behaviour is as expected [57].

These results are independent of frequency. In order to gain spectral insight from these emission cones, we will need to apply some variable bandpass filters to the output.

Bandpass filter

A bandpass filter acts to eliminate, or strongly attenuate frequencies outside a certain range. This range, or frequency "band" is allowed to "pass" unobstructed. For ease of calculation, we will apply a spectral bandpass filter with a Gaussian profile [54]

$$\Lambda(\omega) = \exp\left(-\frac{(\omega-\omega_0)^2}{2\sigma^2}\right), \tag{2.33}$$

where $\Lambda(\omega)$ is centred around ω_0, the central frequency of the downconversion (alternatively, $\lambda_0 = 1064$ nm). The spectral bandwidth (corrected for a Gaussian pulse profile [14]) is defined as:

$$\sigma = \frac{\Delta\omega}{2.355}, \tag{2.34}$$

where $\Delta\omega$ is the FWHM of the Gaussian. This Gaussian spectral filter can be multiplied onto the pump profile and joint spectral distribution in Eq. (2.20) and integrated as previously described.

For varying bandpass filters we see in Fig. 2.6 that the spatial intensity distribution widens with increasing spectral bandwidth. For broad-ranged filters, the overall intensity of

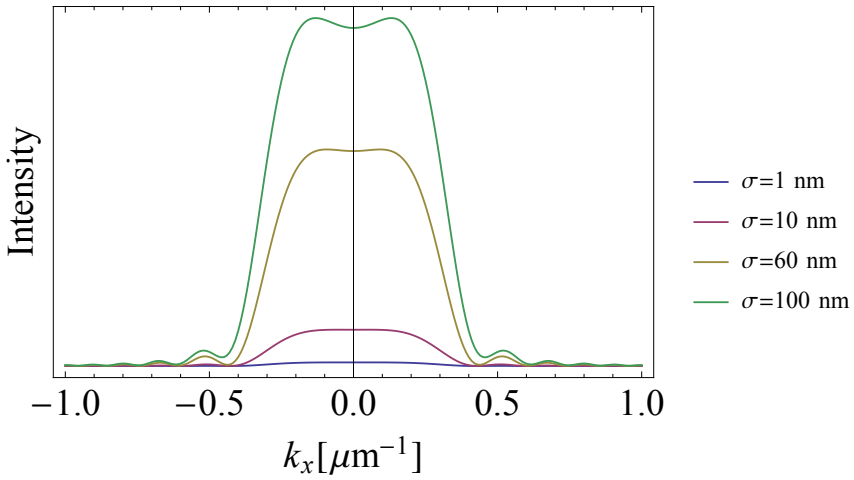

Figure 2.6: Spectral effects on spatial SPDC emission with varied bandpass filtering taken at a beam waist of $w_p = 45$ μm and $T = 26°$C.

the downconversion emission increases, as expected. It is evident that the different spectral bandwidths are equally distributed, concentric cones, containing frequencies farther away from the central frequency. It is interesting to note that $\sigma = 10$ nm and $\sigma = 60$ nm are nearly the same. This is most likely because the expected spectral bandwidth of the process is 60 nm and the spatial distribution of the beam-like downconversion is the same. When frequencies outside of the expected bandwidth are included, larger and larger cone half-angles occur, as seen in Table 2.1.

Table 2.1: SPDC emission half-angles calculated from the FWHM of different spectral bandpass functions in Fig. 2.6.

σ [nm]	α_{air} [°]
10	1.00
60	1.01
80	1.06
100	1.10

Fig. 2.7 shows the temperature dependence on the spatial emission at a beam waist of $w_p = 45$ μm and a bandpass filter of $\sigma = 10$ nm. With spectral filtering, the SPDC emission at the degenerate temperature (26°C) is closely centred around the central frequency. At temperatures beneath the degenerate temperature, phasematching is more prominent at larger opening angles. One could argue that the half-angle pertaining to a certain ω_0

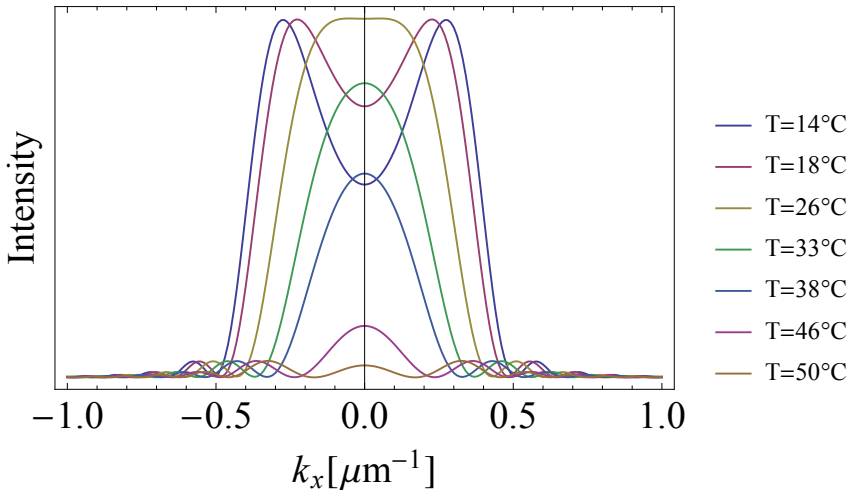

Figure 2.7: Temperature variations on spatial SPDC emission with a 10 nm bandpass filter taken at a beam waist of $w_p = 45$ μm and $T = 26°$C.

decreases with increasing temperature.

Finally, the variation of beam waist under a 10 nm bandpass in Fig. 2.8 is similar to that of Fig. 2.5. The bandpass limits the frequencies measured, thus the maximum opening angle. A tighter beam waist again shows a larger SPDC intensity.

In the next section, we will compare the behaviour of a simulated 10 nm bandpass filter with experimental spatial downconversion images obtained on a standard beam profiler.

2.2.3 Comparison with experimental data

In the lab, it was observed that the spatial profile of the downconversion: a) could be imaged on a standard CCD beam profiler, and b) was not a collinear, single-mode beam as initially expected. The use of the CCD camera became an integral tool in further alignment. In the following section, we will characterize Type 0 SPDC through experimental and theoretical means.

Experiment description

High flux downconversion was obtained by pumping a PPLN crystal with 1 W cw of 532 nm. It was expected that this Type 0 beam-like collinear downconversion would produce a beam diameter of 4.4 mm at the $f = 100$ mm collimating lens. Given that this beam should fit in its entirety on the beam profiler's 6.3 mm $\times$ 4.8 mm active area, it came as a surprise as the whole chip displayed clipping from the ∅1" filter optics.

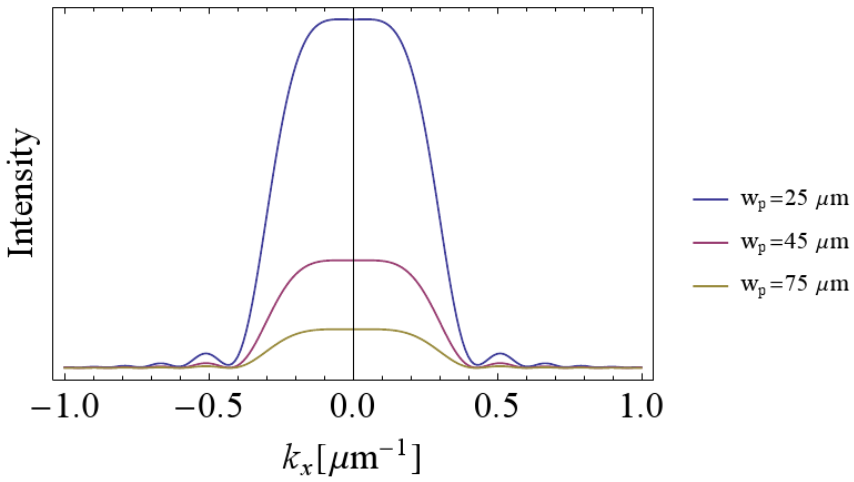

Figure 2.8: Beam waist on spatial SPDC emission with FWHM bandpass of 10 nm taken at $T = 26°C$.

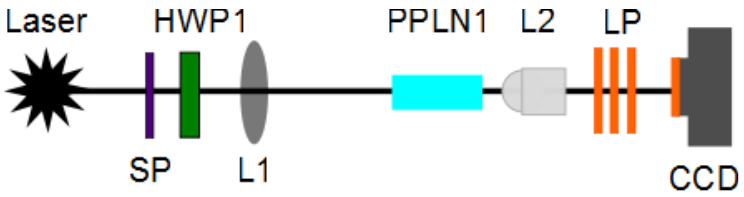

Figure 2.9: Experimental diagram for spatially profiling 1064 nm downconversion created from focusing a $f = 100$ mm lens (L1) into a PPLN crystal (PPLN1) and collimating with an Olympus PLN 10x objective (L2). The 1 W of 532 nm pump is filtered with long-pass 776 nm filters before the WinCamD beam profiler (CCD).

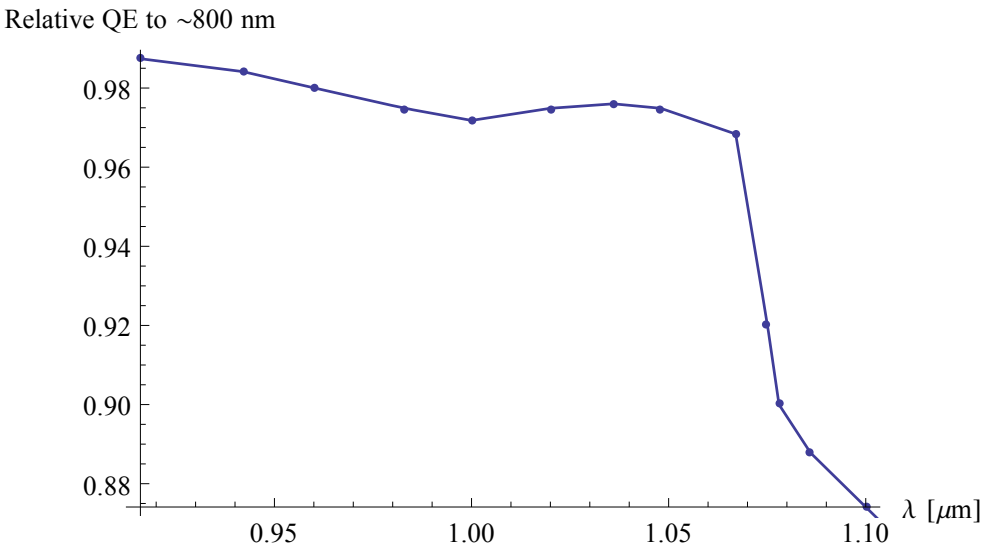

Figure 2.10: Interpolated and estimated beam profiler detection efficiency relative to $\approx$ 800 nm (maximal efficiency). [58]

With the proper choice of collimating lens (10x objective, $f = 16$ mm), the conical structure was able to be investigated within the limits of the beam profiler, following the experimental setup seen in Fig. 2.9. The polarization of the pump beam was set to vertical using HWP1. In total, four Semrock FF01-776/LP-25 long pass filters were used at 0° incidence to remove the roughly 1 W of 532 nm before the unattenuated beam profiler. Three filters were mounted after the crystal, and one was directly attached to the beam profiler to reduce stray background light. The optimal position of the objective was obtained by comparing the size of the downconversion at locations in the near- and farfield (60-70 cm). The focus position inside the crystal also had a large effect on the beam size. By alternating adjustments to the lateral crystal position and collimating objective position in the near and farfield, respectively, a crisp and near collimated downconversion beam size could be obtained. The tip/tilt of the crystal could be adjusted to minimize clipping of the cone on the resistive heater, but not to change the opening angle of the cone.

The beam profiler cannot spectrally distinguish the broadband downconversion emission. However, as discussed in Fig. 2.10, the spectral response is not optimized, nor is it constant over the wavelengths of interest. Because the relative quantum efficiency of the beam profiler plummets just higher than the centre wavelength, 1064 nm, the raw intensity image is misleading due to lower wavelengths being favoured. Spectral information from the cone could only be obtained from inserting separate narrowband spectral filters.

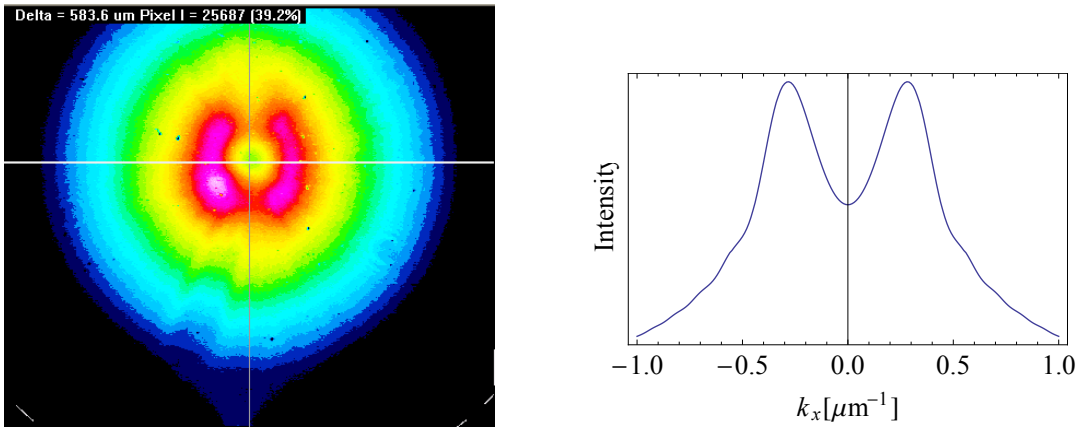

(a) Experiment (b) Simulation

Figure 2.11: Beam profile of SPDC emission for $T = 25°C$ and $w_p = 45$ μm for a corrected poling period, $\Lambda = 6.965$ μm. The calculated half angles: a) $(2.00 \pm 0.02)°$, b) $2.59°$. Spatial profile imaged under different conditions than Fig. 2.12.

Results

The unfiltered downconversion beam profile is displayed in Fig. 2.11a. Under the assumption that the downconversion is properly collimated, the lens focal length and the size of the CCD beam profiler chip can be used to calculate the half angle of the downconverted beam. It should again be mentioned that lower wavelengths will be detected at a higher rate than higher wavelengths. From prior analysis in the previous sections, we know that higher wavelengths have smaller half-angles and decrease with temperature. For this reason, it is expected that the angle obtained from the predominant peaks should be larger than predicted. The calculated half angle is $\alpha_{\text{exp}} = 2.00°$ with an angle measurement uncertainty of $0.02°$. However, it is noted that the collimation/lens position uncertainty is much larger, though currently unknown.

In this section, the theoretical results used the effective poling period of crystal ($\Lambda = 6.965$ μm), not the given one ($\Lambda = 6.97$ μm) to better simulate the experimental SPDC. In Fig. B.1a, the FWHM of the emission cone projection is taken, where the half angle is calculated again as per Eq. 2.31 and Eq. 2.32. This value was found to be $\alpha_{\text{sim}} = 2.59°$. In order to get an understanding on the differences between α_{exp} and α_{sim}, the simulated results would need to be convolved with the frequency-dependence on the beam profiler sensitivity. In addition, an uncertainty on the experimental focal length would be beneficial.

A more accurate comparison can be made by inserting a narrow bandpass filter, thus limiting the frequencies visible to the beam profiler. By inserting a 10 nm bandpass filter before the beam profiler, only wavelengths closely centred around 1064 nm are imaged.

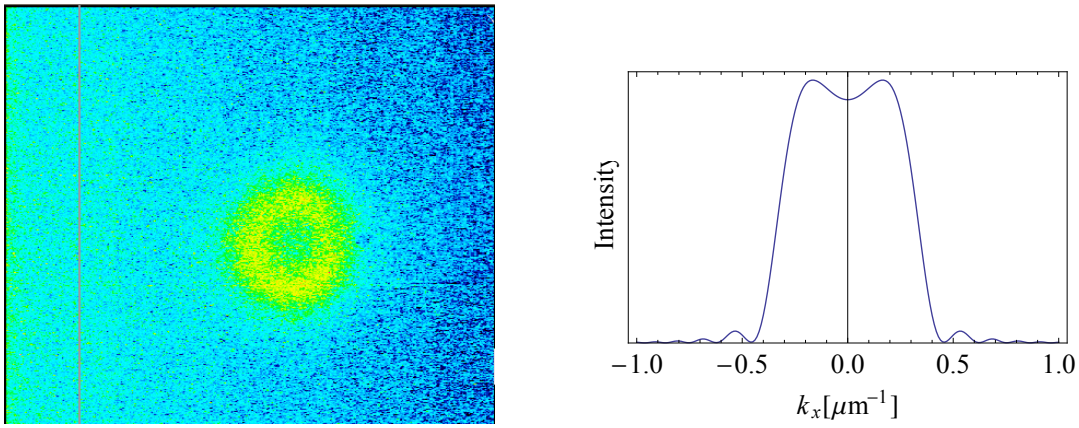

(a) Experiment (b) Simulation

Figure 2.12: Bandpass filter results of the spatial profile of SPDC emission for $T = 25°\text{C}$, $w_p = 45$ μm, and $\sigma = 10$ nm for a corrected poling period, $\Lambda = 6.965$ μm. The calculated half angles: a) $(1.84 \pm 0.02)°$, b) $1.47°$.

For $T = 25°\text{C}$, a ring is observed. Since the degenerate temperature of this crystal is $T = 29.4°\text{C}$, the existence of a ring (or cone) at a lower temperature of $T = 25°\text{C}$ agrees with the simulation predictions of Fig. 2.7.

From the beam profile screenshot in Fig. 2.12a, the experimental half-angle was calculated to be $\alpha_{\text{exp}} = (1.84 \pm 0.02)°$. This value is larger than the simulation result of $\alpha_{\text{sim}} = 1.47°$, as expected due to the detection inefficiency for higher wavelengths, as seen in Fig. 2.10. Since this temperature is below that of the frequency degeneracy, slight noncollinear peaks are evident in Fig. B.1a.

To summarize this section, a greater understanding of Type 0 downconversion from PPLN was established. Simulation results mimic the overall behaviour of the SPDC emission cones, though a one-to-one correspondence has not yet been established. This is expected to be corrected with a convolution of the experimental detection sensitivity with the theoretical results.

This unexpected behaviour may not be detrimental for later SFG or TPA. By using a large enough numerical aperture lens, the full emission cone can be used towards, in this case, upconversion. This may allow for an increased overall efficiency of the total process.

Chapter 3

Ultrafast coincidence detection

Coincidence detection is an integral technique in measuring correlations of light. Light from a source is sent onto a beam splitter and the two output beams are detected on equidistant photodetectors. The time information of the photon "click" signals from both detectors is analyzed to determine if they occurred within a certain time window. Extensive theory has been developed to explain the coincidence statistics gathered from different types of light [59]. The limiting factor of electronic coincidence detection comes from the detectors and coincidence logic. Two-photon processes, such as TPA, require timing windows on the order of femtoseconds, due to the near simultaneity of the events in the process, thus necessitating the concept of "ultrafast coincidence detection". Photon coincidences can occur inside nonlinear media. Examples of such include: atomic vapour, $\chi^{(2)}$ crystals, and molecular dye media, where the "click" signal is equivalent to a fluorescent or parametric photon.

As discussed in Section 1.4, there is an enhancement from energy-time correlated SPDC photons when used in ultrafast coincidence applications. This is due to higher-order field correlations between two beams at certain times and locations. By evaluating the temporal correlations from the energy-time correlated biphoton "source" at a certain location, the second-order correlation function, or $g^{(2)}(\tau)$, can model ultrafast coincidence rates for a variety of two-photon processes.

This chapter will begin with a discussion of optical coherence, followed by examples and definitions of first- and second-order coherence. This thesis concerns coherences in a SPDC source. A brief outline of experimental demonstrations of entanglement-enhanced rates and higher-order interference will also be discussed.

3.1 Optical coherence

Consider Young's double-slit experiment [60, 61]. A source, located behind a screen containing two narrow slits, illuminates a second screen. The resulting intensity distribution exhibits interference fringes, which depend on the slit width and second screen distance; the light intensity on the second screen is not the sum of the individual intensities of the two slits. In order for a fringe pattern to be observed, there must be a *coherence* in the source.

As already mentioned, field correlation functions can demonstrate the spatiotemporal coherences of light. The classical description of coherence can explain most sources of light. However, once we begin to consider the single-photon regime and use nonclassical light sources, a more complete, quantum mechanical description of coherence is needed [59]. Since the nonclassical state of SPDC is of interest, a quantum-mechanical approach is taken in this work.

Correlation functions have a greater use than simply describing light sources with abstract mathematical constructs. In the field of single-photon source development, the goal is to obtain a value of $g^{(2)}(0) = 0$ [62], where only one photon is emitted at a time. The different applications of the second-order correlation[1] function will be discussed.

3.1.1 Quantization of the electromagnetic field

The theory of optical coherence has been well documented [59, 63]. Classical and quantum optical coherence have many similarities, except for the differences arising out of the definition of the electric field (continuous plane wave versus quantized field) [59, 64, 65].

For correlations between detected single-photons and intensities, Glauber's theory of single-photon detection [66] is needed. Further discussion can be found in the following references: [61, 63, 65], among others. This theory is built on the normal-ordering of the electric field to avoid vacuum contributions to the photon intensity detection, and thus detection events without photons incident. The following definitions will be made assuming a quantized electric field with the restriction that the measured intensities be normal-ordered. $(\hat{E}_j^- \hat{E}_j^+)$.

To reiterate Eq. (2.5), a single-mode quantized electromagnetic wave representing pos-

[1] In this work, "first-" and"second-order" coherences refer to intensity correlations. These labels are analogous to "second-" and "fourth-order" coherences, refering to electric fields.

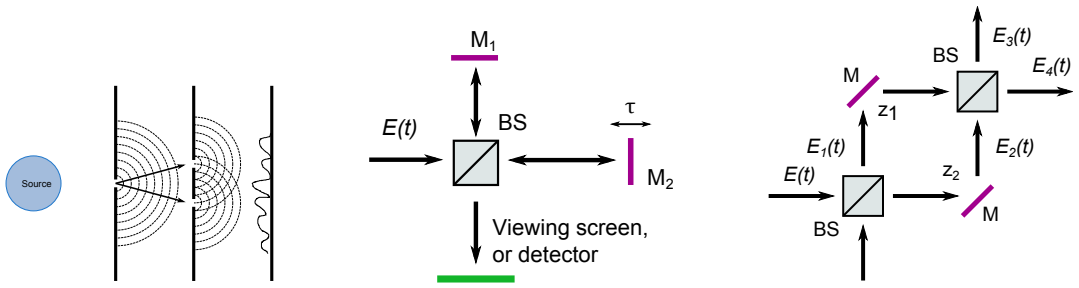

(a) Spatial coherence from Young's double slit experiment

(b) Temporal coherence from a Michelson interferometer

(c) Spatiotemporal coherence from a Mach-Zehnder interferometer

Figure 3.1: Different types of coherences, where in a) the slit is the gap, and in b) and c), BS is a 50:50 beam splitter, and M is a mirror.

itive frequencies is:

$$\hat{E}_j^{(-)} = -i\sqrt{\frac{\hbar\omega_j}{2\epsilon_0 V_Q}}\hat{\varepsilon}_j\hat{a}^\dagger(\omega_j)e^{i(k_{j,z}z-\omega_j t)} \tag{3.1}$$

where j represents the signal or idler, $\hat{a}_j^\dagger$ is the creation operator, and V_Q is the quantization volume. Similarly, its negative frequency component hermitian conjugate is:

$$\hat{E}_j^{(+)} = +i\sqrt{\frac{\hbar\omega_j}{2\epsilon_0 V_Q}}\hat{\varepsilon}_j\hat{a}(\omega_j)e^{-i(k_{j,z}z+\omega_j t)}. \tag{3.2}$$

3.1.2 First-order coherence

Most instances of the term"coherent" are actually examples of first-order coherence [60]. A single transverse-mode laser through a double slit will exhibit fringes due to spatial coherence. A Michelson interferometer can display interference fringes via the temporal coherence of the laser. The Mach-Zehnder interferometer uses both spatial and temporal coherence of the source [65], with interference occurring in two points $(\mathbf{r}_1, t_1)$ and $(\mathbf{r}_2, t_2)$. Examples of these types of coherences can be seen in Fig. 3.1.

Assuming a Mach-Zehnder interferometer is built in the plane ($\mathbf{r}_1 = \mathbf{r}_2$), the intensity of the output, over a temporal cycle of oscillation, is found to be [65]:

$$\langle\hat{I}_4(t)\rangle = \frac{1}{2}\epsilon_0 c|R|^2|T|^2\left\{\langle\hat{E}^{(-)}(t_1)\hat{E}^{(+)}(t_1)\rangle + \langle\hat{E}^{(-)}(t_2)\hat{E}^{(+)}(t_2)\rangle + 2\mathrm{Re}\langle\hat{E}^{(-)}(t_1)\hat{E}^{(+)}(t_2)\rangle\right\}, \tag{3.3}$$

where R/T is the reflectance/transmittance of the beamsplitters. The angle brackets represent quantum mechanical expectation values,

$$\langle \hat{E}^{(-)}(t_1)\hat{E}^{(+)}(t_2)\rangle = \mathrm{Tr}\left\{\hat{\rho}\hat{E}^{(-)}(t_1)\hat{E}^{(+)}(t_2)\right\}, \tag{3.4}$$

where $\hat{\rho}$ is the density operator of the quantum state of light.

The last term of Eq. (3.3) is responsible for interference fringe, which, is used to define the first-order coherence function, written as a time-averaged expectation value of Eq. (3.4).

When dealing with *stationary*, non-pulsed, steady-state (not recently turned on) light where the fluctuations are small compared to the period, we can statistically sample from the light distribution without affecting the outcome. Rewriting Eq. (3.4) in terms of time delay $\tau = t_2 - t_1$, we obtain:

$$\langle \hat{E}^{(-)}(t)\hat{E}^{(+)}(t+\tau)\rangle = \mathrm{Tr}\left\{\hat{\rho}\hat{E}^{(-)}(t)\hat{E}^{(+)}(t+\tau)\right\}. \tag{3.5}$$

The normalized degree of first-order coherence is defined to be:

$$g^{(1)}(\tau) = \frac{\langle \hat{E}^{(-)}(t)\hat{E}^{(+)}(t+\tau)\rangle}{\langle \hat{E}^{(-)}(t)\hat{E}^{(+)}(t)\rangle}. \tag{3.6}$$

Since this distribution is based on the statistical results for stationary light, the only dependence comes from the time delay, τ. This means this complex function is symmetric:

$$g^{(1)}(\tau) = g^{(1)}(-\tau)^*. \tag{3.7}$$

It is obvious from Eq. (3.6) that, for $\tau = 0$, the first-order coherence function evaluates to $g^{(1)}(0) = 1$, and furthermore, $g^{(1)}(\tau) \leq 1$ [59]. For time delays much shorter than the light's coherence time and $\tau \neq 0$, the magnitude of the degree of first-order coherence can characterize the light as:

$$|g^{(1)}(\tau)| \begin{cases} = 1 & \text{first-order coherent,} \\ = 0 & \text{incoherent,} \\ \neq 0 \text{ or } 1 & \text{partially coherent.} \end{cases} \tag{3.8}$$

Other interesting properties of the degree of first-order correlation relates back to the Mach-Zehnder interferometer in Fig. 3.1. Eq. (3.8) has practical application in defining the visibility of the fringes[2].

[2]This is true for either spatial or temporal coherence. The traditional visibility, or fringe sharpness, is calculated as $V = \frac{I_{\max} - I_{\min}}{I_{\max} + I_{\min}}$. By calculating $I_{\max}$ and $I_{\min}$ from Eq. (3.3) (or the output of another type of interferometer), it can be seen that the modulus of the "mutual coherence" or "autocorrelation" term (Eq. (3.4)), is the visibility, $V = |g^{(1)}(\mathbf{r}_1, t_1; \mathbf{r}_2, t_2)|$.

The Mach-Zehnder interferometer can be visualized with a change of variable,

$$\tau = t_2 - t_1 - \frac{z_2 - z_1}{c}, \tag{3.9}$$

where the measured point of correlation takes place at space-time coordinates, (z_1, t_1) and (z_2, t_2), assuming the interferometer is perfectly in the plane.

3.1.3 Second-order coherence

The degree of first-order coherence looks at correlations between fluctuations in the electric field. The extension to higher-order correlations can simply be seen as correlations in *intensity*, not electric field. The degree of second-order coherence, for stationary, single-polarization light is:

$$g^{(2)}(\tau) = \frac{\langle \hat{E}^{(-)}(t)\hat{E}^{(-)}(t+\tau)\hat{E}^{(+)}(t+\tau)\hat{E}^{(+)}(t)\rangle}{\langle \hat{E}^{(-)}(t)\hat{E}^{(+)}(t)\rangle^2}. \tag{3.10}$$

This higher-order coherence signifies the ability for intensities of light to interfere at two space-time coordinates, (z_1, t_1) and (z_2, t_2).

$$g^{(2)}(z_1, t_1; z_2, t_2) = \frac{\langle \hat{E}^{(-)}(z_1, t_1)\hat{E}^{(-)}(z_2, t_2)\hat{E}^{(+)}(z_2, t_2)\hat{E}^{(+)}(z_1, t_1)\rangle}{\langle \hat{E}^{(-)}(z_1, t_1)\hat{E}^{(+)}(z_1, t_1)\rangle\langle \hat{E}^{(-)}(z_2, t_2)\hat{E}^{(+)}(z_2, t_2)\rangle} \tag{3.11}$$

The numerator of the $g^{(2)}$ must be positive [59], thus the range of possible values can be (for both $\tau \neq 0$ and $\tau = 0$):

$$0 \leq g^{(2)} \leq \infty. \tag{3.12}$$

This differs from the classical range of the $g^{(2)}$ where $1 \leq g^{(2)}(0) \leq \infty$ and $g^{(2)}(\tau) \leq g^{(2)}(0)$ [65].

The expression in Eq. (3.11) is written with all field operators originating in the same beam, meaning it refers to *intrabeam* correlations, as opposed to *interbeam* correlations between two beams. Rewriting Eq. (3.11) in terms of distinct modes, assuming measured at the same location [65]:

$$g^{(2)}_{l,m}(t_1, t_2) = \frac{\langle \hat{E}^{(-)}_l(t_1)\hat{E}^{(-)}_m(t_2)\hat{E}^{(+)}_m(t_2)\hat{E}^{(+)}_l(t_1)\rangle}{\langle \hat{E}^{(-)}_l(t_1)\hat{E}^{(+)}_l(t_1)\rangle\langle \hat{E}^{(-)}_m(t_2)\hat{E}^{(+)}_m(t_2)\rangle}, \tag{3.13}$$

where $l, m = a, a$ or b, b refers to intrabeam degrees of coherence

where $l, m = a, b$ or b, a refers to interbeam degrees of coherence

The difference between inter- and intrabeam correlations in second-order degrees of coherence are commonly confused. We will discuss differences between the two, followed by its relation to entanglement-enhanced ultrafast coincidence detection.

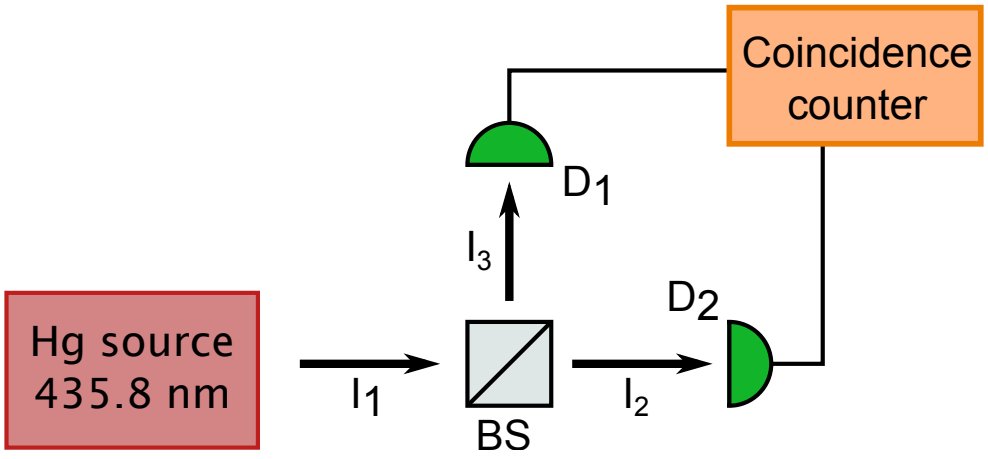

Figure 3.2: A simplified Hanbury Brown Twiss interferometer for measuring intrabeam second-order intensity correlations, assuming symmetric detector distances.

Intrabeam correlations

The famous experiment by Hanbury Brown and Twiss (HBT) [67] measured second-order intrabeam correlations using coincidence detection, as seen in Fig. 3.2. The time-averaged intensities of the resulting two beams were measured from a single source of 435.8 nm light incident on a 50:50 beamsplitter. If the relative beam time delay was less than the coherence time of the source, $\tau < \tau_c$, then the intensity fluctuations of the light source can be measured. However, for very low coherence time sources, such as used in this work, single-photon detectors are not fast enough, thus detection through nonlinear frequency conversion is often used.

As mentioned previously, the single-photon nature of quantum dots is characterized via intrabeam intensity correlations [62], $g^{(2)}_{a,a}(0) = 0$. This performance parameter is also used for perfect heralded (triggered) single-photon generation from SPDC. This is measured by separating one photon, for example the signal photon, from a SPDC biphoton source, and using it as a trigger while the idler photon undergoes HBT interferometry [68, 69], similar to Fig. 3.2.

Interbeam correlations

Interbeam correlations require the photons be relatively manipulatable in distinct modes, such as orthogonal polarizations, non-overlapping frequencies, spatially separate, or different phase. Relevant for this work, we will see later that we can take "interbeam" to refer to correlations between signal and idler photons from SPDC biphoton pairs, not neces-

sarily photons within distinct beams. Interbeam intensity correlations, also called cross-correlations, are more difficult to measure due to limitations in detector time sensitivity, especially for short coherence length light. In the last decade, advances have been made towards using nonlinear media interactions, such as SFG, or TPA [68, 70, 71] to measure interbeam coherence. One experimental cross-over technique between HBT interferometry and frequency conversion was the experiment of Boitier *et al.* [69, 72] in performing TPA within the semiconductor of the detector, thus allowing for the required ultrafast timing window.

Interbeam intensity correlations between signal and idler SPDC photon are of interest for studying the role of energy-time entanglement in time-resolved coincidences. When one investigates the second-order interbeam coherences of these frequency-correlated pair states, we, in fact, find the very goal of this chapter: a function describing the rate for two photons meeting in both time and space [73].

With advances in nonlinear materials (such as quasi-phasematching, Section 2.1.2), single-photon-level SFG became possible [23]. By using broadband fields, the single-photon number per mode can still be less than unity (thus maintaining nonclassical properties) while high flux can be used to obtain adequate SFG signal from the low conversion rates.

3.2 Entanglement-enhanced ultrafast coincidences

As was outlined in Section 1.4, SPDC photons lead to increased ultrafast coincidences in nonlinear media over coherent ultrafast lasers [20]. In this section, we will explore how the second-order correlation function is proportional to the ultrafast coincidence rate. Furthermore, we will outline how the properties of SPDC can allow for increased second-order correlations, and subsequently, larger ultrafast coincidence rates. Examples of experiments using entangled biphotons demonstrating an increased ultrafast coincidence rate as well as higher-order correlations will be discussed. The concept of an entangled light microscope will also briefly be revisited.

3.2.1 Second-order correlations from an SPDC source

Burnham and Weinberg [74] showed that maximal coincidences between signal and idler photons from SPDC occur when the time delay between the two are the same, and phase-matching conditions conserved ($\omega_p = \omega_s + \omega_i$ and $\mathbf{k_p} = \mathbf{k_s} + \mathbf{k_i}$). The inherent temporal and spatial [56] correlations between signal and idler photons are related through many

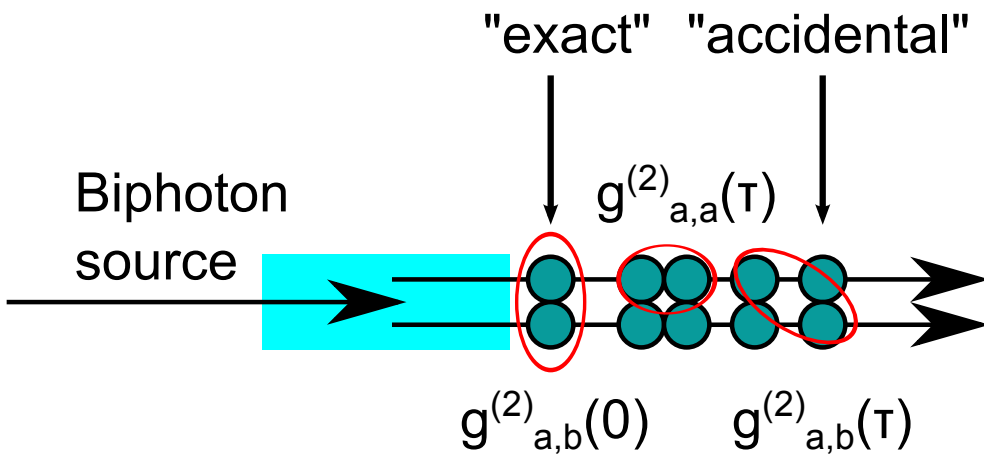

Figure 3.3: Second-order interbeam ($g^{(2)}_{a,b}(\tau)$) and intrabeam ($g^{(2)}_{a,a}(\tau)$) correlations. These higher-order coherence effects can only be measured by ultrafast detectors, such as through SFG and TPA. Due to the spatiotemporal properties of SPDC, the "exact" interbeam correlations are much more likely than the random "accidental" interbeam correlations.

parameters, including: pump pulse duration, crystal length, pump beam waist, and crystal structure [75, 76].

The $g^{(2)}_{a,b}(\tau)$ is proportional to the probability of detecting either the signal (or the idler) photon at a certain $t+\tau$ after the idler (or signal) photon is measured at time t. This means that the interbeam correlation can measure to what extent the signal and idler are part of a pair [69]. As seen in Fig. 3.3, the well-defined temporal correlations within pairs will lead to a larger $g^{(2)}_{a,b}$ than the"accidental" coincidences from photons in other pairs. According to Dayan [22], "coherent" contributions correlations are proportional to the "exact" $g^{(2)}_{a,b}(\tau)$, and the "incoherent", the "accidental". The inherent spatial and temporal correlations in SPDC allow for a linear, rather than quadratic, ultrafast coincidence rate, as outlined in Section 1.4.

In the experiment outlined in the following chapter, the ultrafast coincidence process of SFG is designed to demonstrate enhancements from interbeam correlations. However, the SPDC source described is frequency degenerate, Type 0 (same polarization), and exhibits a beam-like spatial mode, as described in the previous chapter. It would seem that this lacks the distinct, separable mode interbeam correlations requires. However, since the signal and idler photons are created from separate frequency-dependent creation operators, $\hat{a}(\omega_s)$ and $\hat{a}(\omega_i)$, we can artificially split the degenerate, broadband spectrum into a lower and higher frequency "modes". Since the correlation between the signal and idler is of interest – and since they sum parametrically to the pump frequency – we can describe this SPDC source using degree of second-order interbeam coherence.

Since SPDC and the ultrafast coincidence process (SFG or TPA) are inefficient processes, very large pump powers (> 1 W), and thus, high fluxes of downconversion (≈ 1 μW) are used. By having spectrally large bandwidth downconversion [23], where

$$\Phi_{\max} \approx \Delta\nu_{\mathrm{DC}} \tag{3.14}$$

will result in maintaining single-photon frequency conversion: for $\Delta\lambda_{\mathrm{DC}} = 60$ nm downconversion centred around 1064 nm, $\Delta\nu_{\mathrm{DC}} = 16$ THz, thus leading to $P_{\max} = 3$ μW. This allows the downconversrion to be viewed as single photon per mode when the spectral mode density is $n = \frac{P}{P_{\max}} \leq 1$.

3.2.2 Examples of entanglement-enhanced coincidence detection

In order to probe higher-order correlations of nonclassical light, such as SPDC, exceedingly fast timing resolution ($\approx$ fs) is needed. Since current detector technology exists, at best, in the picosecond regime, two-photon nonlinear material "detectors" are necessary.

In this section, we will discuss relevant experiments which demonstrate this entanglement enhancement from the biphoton wavefunction in an ultrafast measurement of the $g^{(2)}_{a,b}(\tau)$, as well as other ultrafast coincidence measurements which show manipulation of this correlation function through second-order interference.

The nonclassical rate enhancement was first demonstrated by Dayan *et al.* [23]. Broadband, high flux downconversion, showed a linear ultrafast coincidence rate through upconversion in a nonlinear crystal. This experiment was completed without variations of signal and idler time delay, thus $g^{(2)}_{a,b}(0)$ was measured for varying powers showing the great potential of SPDC entanglement enhancement. O'Donnell and U'Ren [77], using a piezo-controlled half mirror, measured the time-resolved upconversion of downconversion, and thus, $g^{(2)}_{a,b}(\tau)$. A two-photon absorption example was demonstrated by Dayan *et al.* [78], where the high-powered downconversion (squeezed vacuum) was split, where the signal underwent spectral phase manipulation with a SLM and variably delayed before recombination with the idler photon within a rubidium cell.

These intrinsic coherences can also lead to second-order interference effects in time and space [79, 80]. Since our ultimate goal is entanglement-enhanced ultrafast coincidences in nonlinear media, a good intermediate example is seen again in the experiment of Boitier *et al.* [69], using clever interferometry before detecting interference fringes in ultrafast coincidences via TPA in a semiconductor single-photon detector.

A relevant example of second-order interference in photon pairs: SFG was demonstrated by Pe'er *et al.* [81] with a nonlinear crystal. In this experiment, the GVD was

compensated by a four prism compressor with a SLM in the middle to exhibit coherent spectral phase control on high flux, large bandwidth downconversion. This allowed for second-order interference fringes to be measured in the upconversion signal ($g^{(2)}_{a,b}(\tau)$). An interesting application of this to the field of quantum information was demonstrated by Bernhard *et al.* [82], where, in a similar setup, spectral phase manipulation was used to create frequency qudits (quantum states) frequency-entangled up to dimension $d = 4$, and using upconversion as a projective measurement. The second-order interference in this experiment is seen in the resultant spatiotemporal overlap (in the nonlinear crystal) from specific phase shifts applied by a SLM to non-overlapping frequency bins.

Higher-order correlations have been of interest in the last decade. With this technology now well established, we can hope that more practical applications of entanglement-enhanced coincidences, such as an entangled light microscope, can be achieved in the coming years.

Chapter 4

Experiment

In this chapter, we will discuss the makings of an experiment, similar to that of O'Donnell and U'Ren [77]. This was built in order to probe entanglement-enchanced ultrafast coincidences through the nonlinear process of SFG as an intermediate step towards ETPA. By obtaining a grasp for femtosecond coincidences in a PPLN crystal, the necessary skills can be gained before moving on to a two-photon absorbing medium.

This experiment has been a long time in the making. The chronological journey of this project, leading to the current ideas and knowledge displayed in this work, is communicated in pictorial form in Appendix B.

The main components of the entire experiment, in its current form, is displayed in Fig. 4.1 and will be characterized in the subsequent sections. Comments and recommendations for this current experiment will also be suggested.

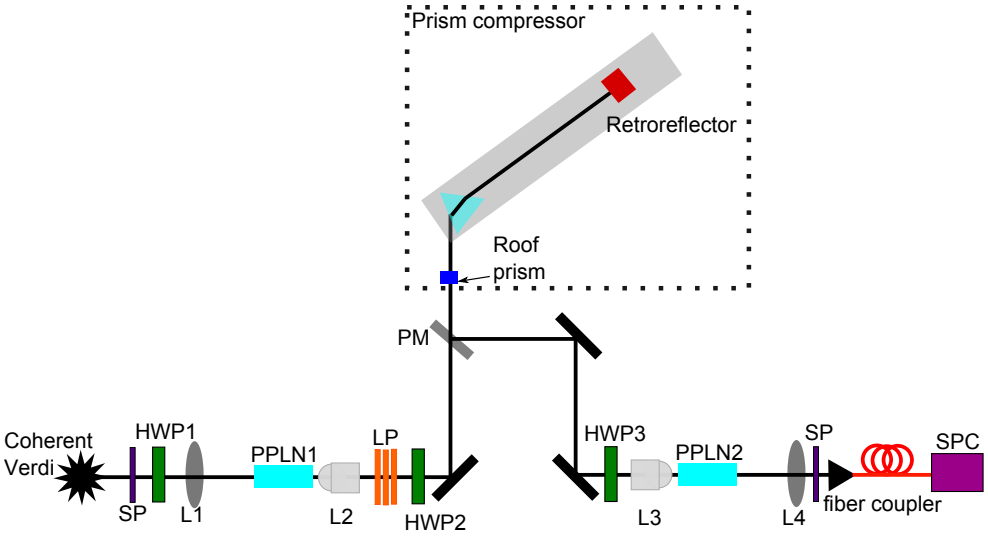

Figure 4.1: Complete experimental upconversion of downconversion setup to be characterized. Photon pairs, centred around 1064 nm, are created from focusing a pump beam through a $f = 100$ mm lens (L1) into a PPLN crystal (PPLN1) and collimating with an Olympus PLN 10x object (L2). The 1 W of 532 nm pump is filtered with a short-pass 650 nm filter prior to entering the setup. After the crystal, the 532 nm pump is filtered using multiple long-pass 776 nm filters (LP). A half wave-plate (HWP2) is used to rotate the polarization to horizontal before passing through a quadruple-pass prism compressor and being picked off by overhanging pick-off mirror (PM). HWP3 is used to rotate the polarization back to vertical before the reverse process is then traversed where the SPDC pairs are focused, using L3, into PPLN2 and collimated, using L4=L1. A shortpass 720 nm filter (SP) is used to allow only the upconverted signal to pass into the single-photon counter (SPC).

4.1 Ultrafast cw source for ETPA

The nonlinear material of interest in this work is PPLN. Briefly, we will outline reasons behind this choice before discussing characteristics of this crystal in SPDC.

Certain design considerations were made when choosing the crystal specifications:

1. Able to withstand high pump power
2. Engineered for broadband SPDC from 532 nm $\rightarrow$ 1064 nm
3. Long enough to be efficient, yet short enough not to accumulate large amounts of GDD.

As previously mentioned in Section 3.2.1, it is possible to have very high fluxes of spectrally broadband downconversion while still remaining in the single-photon-per-mode regime. For this source, the maximum single-photon-per-mode downconversion intensity is 3 μW which is about three times larger than experimental conditions. To cope with the high powers, it has been found that Mg:O-doping of LN has allowed for increased damage thresholds [83]. The chosen downconversion and upconversion crystals (designated "PPLN1" and "PPLN2", respectively) contained the properties displayed in Table 4.1.

Table 4.1: Given specifications of 5% MgO-doped PPLN crystals

Poling period, Λ	Crystal length, L
6.97 μm	5 mm

During the course of this project, it was found that PPLN is a highly dispersive material, where 5 mm can accumulate 1363 fs^2 of GDD at $\lambda = 1064$ nm. This is comparable to that of an average microscope objective lens [84]. Since downconversion can occur over the whole length of the crystal (though most probable in the central focus), it becomes problematic when GDD, at best, can only be compensated for one point. This means that it is not possible to compensate all downconversion photons emitted from the crystal. Arguably this is one of the larger sources of dispersion in entanglement-enhanced ultrafast coincidence experiments [77].

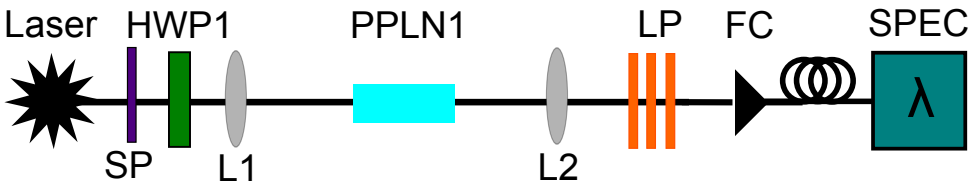

Figure 4.2: Setup for investigating the phasematching 1064 nm downconversion created from focusing a pump beam by a $f = 100$ mm lens (L1) into a PPLN crystal (PPLN1) and collimating the beam with a $f = 100$ mm lens (L2). Any unfiltered infrared photons remaining in the 1 W of 532 nm pump are filtered using a short-pass filter (SP). After the crystal, the pump beam is removed using long-pass 776 nm filters (LP) before the remaining downconversion is fibre coupled (FC) and detected with a spectrometer (SPEC).

4.1.1 Spectrum

Previously, the spatial distribution of SPDC emission was discussed in Section 2.2.3. In this section, the spectral emission will be compared. The experimentally determined phasematching will be compared to the theoretically modelled phasematching.

The first task of characterizing a new downconversion crystal is to determine the phasematching curve and degeneracy temperature. A configuration similar to Fig. 4.2 was used to generate, then later fibre-couple, most of the downconversion into a multimode (MM) fibre to be analyzed via spectrometer. Due to the downconversion emission having a very large spectral bandwidth (FWHM $\approx$ 60 nm), it was only possible to accurately distinguish the centre wavelengths of the signal and idler photons when they were adequately frequency nondegenerate, as seen in Fig. 4.3. Downconversion collected over a range of temperatures allowed for the phasematching curve to be established. From the behaviour of the nondegenerate signal and idler over temperatures, the degeneracy temperature is estimated, via interpolation, to be $T = 29.4°\text{C}$.

The joint spectral density function from Eq. 2.22 can be plotted using the exact uniaxial crystal phasemismatch from Eq. (2.29). Given the poling period specified with the crystal in Table 4.1, it was noted in Fig. 4.4a that the expected degeneracy temperature was 3°C lower than the experimental value. Similarly, in Fig. 4.4b, the specified poling period is 0.005 μm longer than the maximum phasemismatch from Eq. (2.29) in Fig. 4.4. This could point to inconsistencies in the poling period over the length of the crystal, creating an effective poling period of $\Lambda_{\text{eff}} = 6.965$ μm. Alternatively, the Sellmeier equations [83, 85] used to simulate the crystal could be describing the crystal of interest inaccurately.

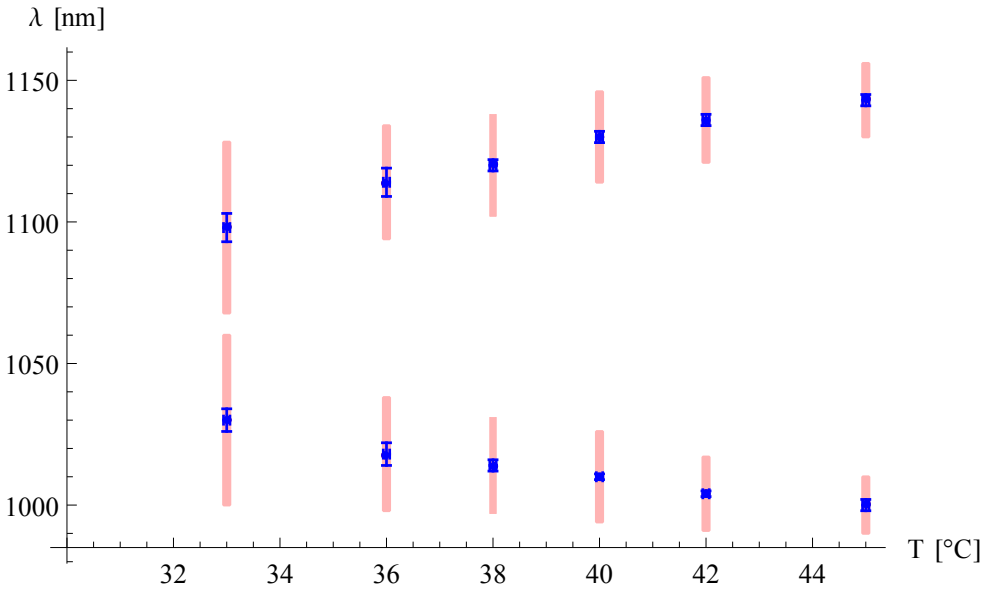

Figure 4.3: Measured phasematching spectrum of SPDC from PPLN with $\Lambda = 6.97$ μm. Interpolation yields a degenerate temperature of $T = 29.4$°C. Red bars represent the experimental spectral bandwidth taken at the FWHM.

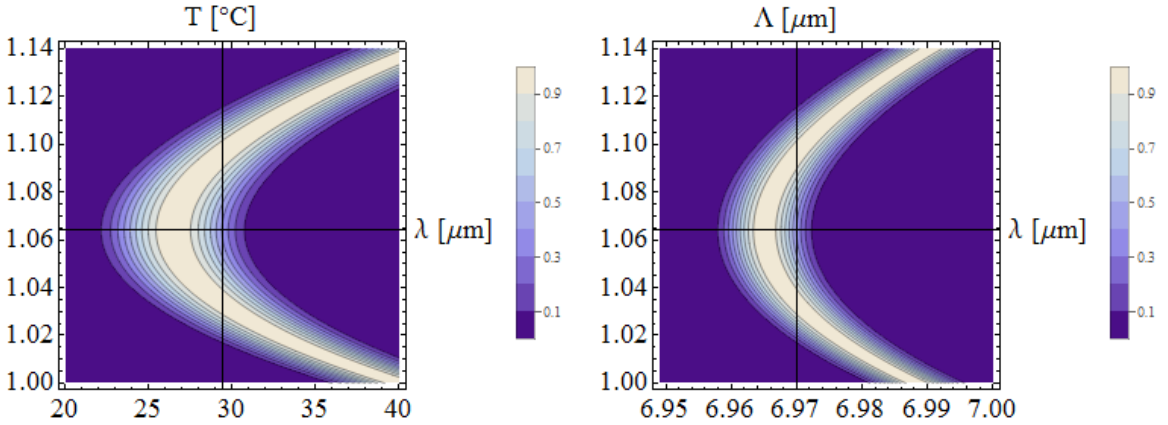

(a) Temperature dependence calculated with $\Lambda = 6.97$ μm; compared with experimental $T = 29.4$°C.

(b) Poling period dependence calculated with $T = 29.4$°C; compared with specified $\Lambda = 6.97$ μm.

Figure 4.4: Simulated phasematching using the uniaxial phasemismatch compared with given experimental parameters.

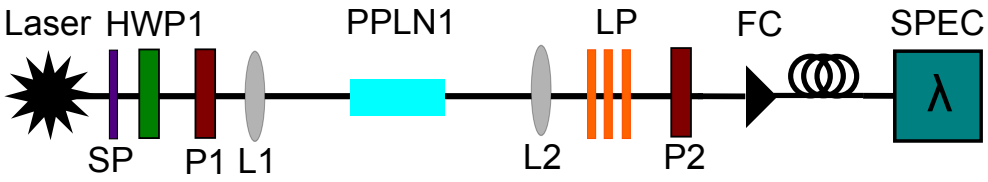

Figure 4.5: Setup for investigating polarization dependence on 1064 nm downconversion created from focusing the pump beam with a $f = 100$ mm lens (L1) into a PPLN crystal (PPLN1) and collimating the beam with a $f = 100$ mm lens (L2). The 1 W of 532 nm pump is filtered with long-pass 776 nm filters (LP), letting the downconversion pass through before being collected into fibre via fibre coupler (FC) and analyzed in a spectrometer (SPEC). Polarizers P1 and P2 were calibrated before and set to different combinations in the horizontal (H) and vertical (V) basis.

4.1.2 Polarization dependency

SPDC is a polarization-dependent process, as previously discussed in Section 2.1.1. Linear polarizers, before and after the crystal, were used to verify the polarization, as seen in Fig. 4.5. The spectrometer used (Acton SpectraPro-750i) had a silicon detector which had a large drop in quantum efficiency after ≈ 1100 nm. For this reason, the crystal temperature was raised to $T = 33.8°\text{C}$ as to produce nondegenerate downconversion, as predicted in Fig. 4.3. This allowed for the lower-wavelength photon to be accurately detected.

Type 0 downconversion in PPLN is supposed to work with "eee" polarizations. In the lab frame, this means that vertically polarized pump photons will produce vertically polarized signal and idler twin photons. To test this, linear polarizers, P1 and P2, were independently rotated between all combinations of vertical (V) and horizontal (H) polarizations. The result of this is seen in Fig. 4.6. As expected, there was only "signal" photons when both P1 and P2 were set to allow vertical polarization to pass through.

This polarization control is a useful characteristic as it allows the downconversion to be "turned off". This is a useful tool for verifying if future entanglement-enhanced TPA or SFG signals are from downconverted photon pairs, rather than stray background light. Unlike other types of downconversion in other crystals, there is no fixed temperature in which below it phasematching does not exist. This is evident in Fig. 2.4 where, instead, for temperatures beneath phasematching, the emission becomes less collinear.

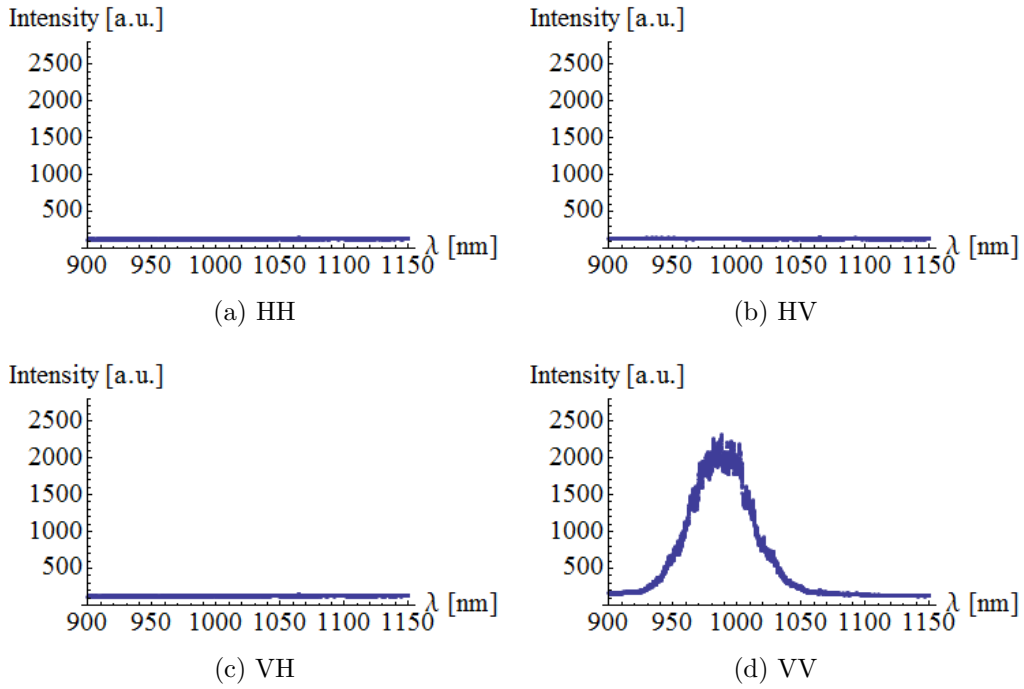

(a) HH

(b) HV

(c) VH

(d) VV

Figure 4.6: Downconversion polarization dependence taken at nondegenerate frequency temperature of $T = 33.8°\text{C}$. For polarizers placed in a SPDC setup according to Fig. 4.5, the polarization dependence of Type 0, "eee" SPDC is confirmed.

4.2 Prism compressor

As discussed in Section 1.3.3, the prism pulse compressor is the least lossy of the typical dispersion compensation methods. The four-prism configuration of a prism pulse compressor was first demonstrated by Fork *et al.* [86]. This solved the problem of spatial transverse displacement of the compressed pulses. This configuration, however, is tricky to align as identical angles and distances between the first- and second- prism, and the third- and fourth- prism, must be maintained at all times (Fig. 1.5). If not, the propagating pulses acquire spatiotemporal distortions.

The complexity can be simplified by placing a tilted mirror after the second prism, requiring only two prisms. This results in the prism compressor being folded in half. However, spatiotemporal distortions can still occur due to angular differences between the two prisms. An interesting alternative to this is to fold the two prism compressor once more, as suggested by Akturk *et al.* [87]. In this configuration, only one prism is used with four beam passes. An experimental example of this is seen in Fig. 4.7. After the first pass through the prism (at Brewster's angle), the beam is sent back via a retroreflector. Because the retroreflector rotates the beam in reflection, the colours are reversed allowing the second pass through the prism to mimic that of the antiparallel traditional second prism. The third pass uses a roof prism which preserves the colour order upon reflecting. This is analogous to the space between the second and third prism. The final reflection through the retroreflector replicates the action of the third and fourth prism, allowing the compressed beam to emerge in the same spatial mode, but temporally compressed. This is advantageous because the retroreflector reflects the beam exactly parallel to its input, to be incident on the original prism at the same angle. This configuration also limits beam magnification through the compressor [87].

Due to the double-folding of the prism compressor, a modification of the prism tip-to-tip distance needs to be made to Eq. 1.21. $L = 2q + \Delta x$, where q is the prism tip to retroreflector distance and Δx is the constant offset within the retroreflector.

Given the different optical materials the broadband downconversion passes through before the second sample, the total dispersion in the current system can be calculated. Using the GVD equation, Eq. 1.11, multiplied with the length of each optic, the GDD of the infrared setup is calculated to be 3287 fs^2. Largest contributing dispersive components are: the latter half of PPLN1 and the first half of PPLN2 (1363 fs^2), and the two Olympus PLN 10x objectives collimating and focusing the downconversion (742 fs^2 each, totalling 1484 fs^2). A theoretical calculation of dispersion for all optical components in this experiment can be found in Table 4.2

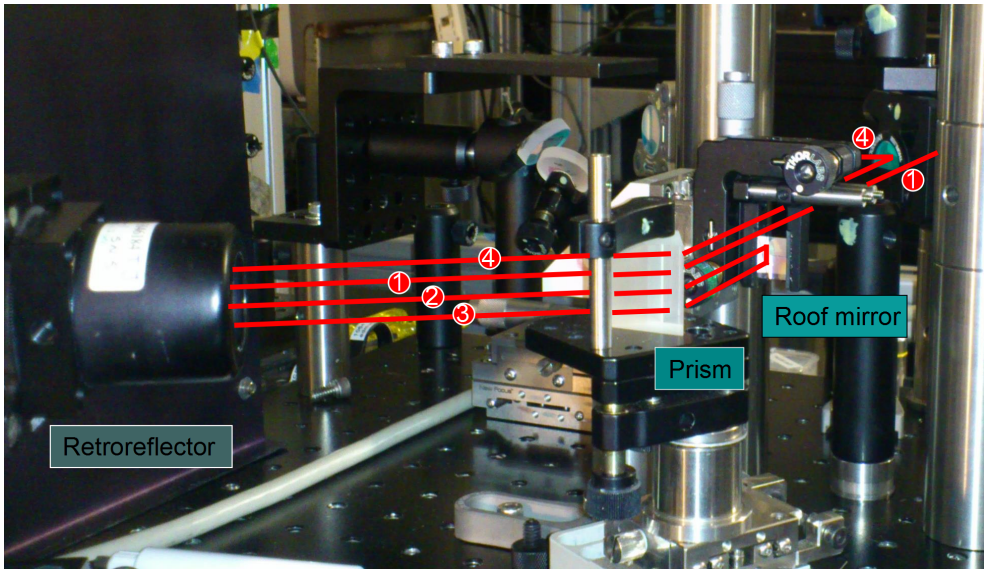

Figure 4.7: Annotated experimental quadruple-pass prism compressor made with a SF10 glass Brewster angle dispersive prism where GVD can be tuned via moving a retroreflector on an optical rail.

Putting it all together, to compensate for the material GDD, the retroreflector-prism distance is calculated to be 16.9 cm. Calculation examples of unfolded prism compressors can be found in Table 4.3.

The overall dispersed pulse behaviour from Eq. (1.20) in a pulse compressor is plotted in Fig. 4.8. Here we see that when the compressor contribution and the material phase contribution to the pulse width are equal and opposite, the pulse is transform-limited.

Table 4.2: Sources of dispersion from optical components within the experiment calculated at $\lambda = 1064$ nm.

	GDD [fs^2]
Olympus PLN 10x (2)	1484
PPLN crystals	1364
Roof prism	201
Half waveplates	126
Filters (assumed 1 mm NBK7)	112
Total dispersion	3287

Table 4.3: Prism compressor examples calculated using Eq. (1.21)

	L [cm]	λ [nm]	h [mm]	$\frac{d^2 P_{OL}}{d\lambda^2}$	Prism glass
Experiment	39.2	1064	4	-3297	SF10
Example	40.0	800	0	-867	Fused Silica

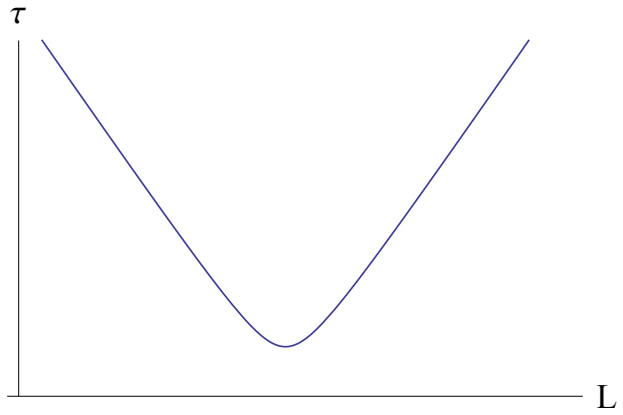

Figure 4.8: Pulse width of a dispersed pulse within a compressor. The minimum of this plot corresponds to the prism compressor location where the pulse is transform-limited. Elsewhere, the excess GVD spreads the pulse width.

4.3 Ultrafast coincidence detector

Given the specific energies of the pump, signal and idler photons chosen for this experiment, semiconductor detector TPA is not the most natural of an intermediate step towards ETPA due to mismatched bandgap energies of most available photomultiplier tubes.

Instead, as a preliminary step towards ETPA, entanglement-enhanced SFG (or in this case, SHG) is investigated. The nonlinear crystal used in this process, PPLN2, is identical to that of the downconversion crystal, PPLN1. In the following sections, PPLN2 will be tuned and characterized as to best facilitate the upconversion of downconversion.

4.3.1 Upconversion spectrum

In order to characterize the crystal, a scanning laser around 1064 nm is needed to tune the the upconversion phasematching to exactly overlap the frequency of the SPDC pump. In this case, a high-speed scanning laser (Santec HSL-2000) was obtained[1] and the upconversion signal was tuned in a setup similar to Fig. 4.11.

The results of the phasematching can be seen in Fig. 4.10. The pink curve represents the Coherent Verdi V-18 pump for the downconversion source. This is exactly centred within the SHG spectrum. This is important as the broadband entangled photon pairs will exactly sum to the frequency of the pump.

A possible cause for the difference in temperature between the processes of SPDC and SHG in identical crystals is that these temperatures are relative, not absolute, as two very different resistive heaters were used for the two crystals.

[1]Many thanks to Dr. Kostadinka Bizheva for lending this laser.

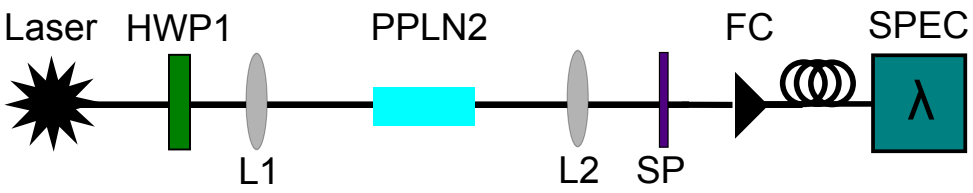

Figure 4.9: Setup for investigating the phasematching on 532 nm SHG created from focusing 0.5 mW of 1064 nm beam with a $f = 100$ mm lens (L1) into a PPLN crystal (PPLN2) and collimating it with a $f = 100$ mm lens (L2). The pump beam is filtered with short-pass 720 nm filters (SP) before being fibre coupled (FC) and analyzed by a spectrometer (SPEC).

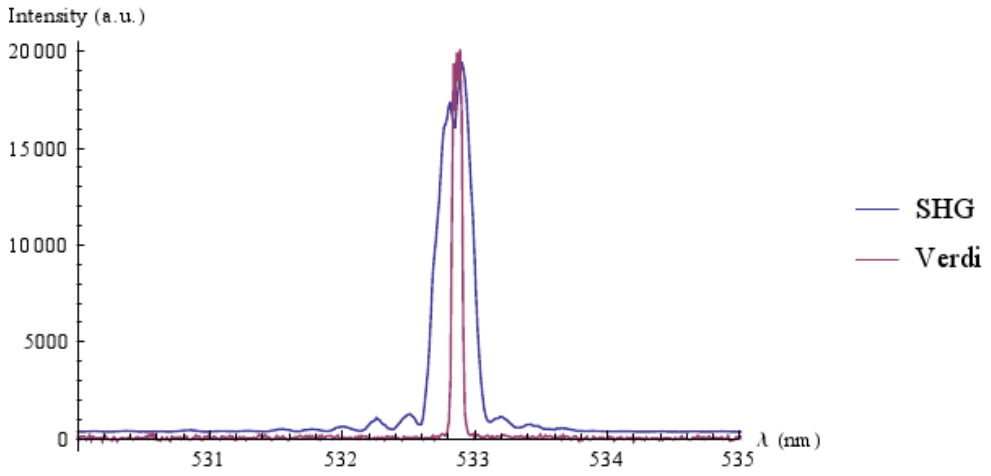

Figure 4.10: Characterization of the PPLN upconversion crystal, temperature tuned to $T = 34.4°\text{C}$ in order to spectrally overlap the downconversion pump.

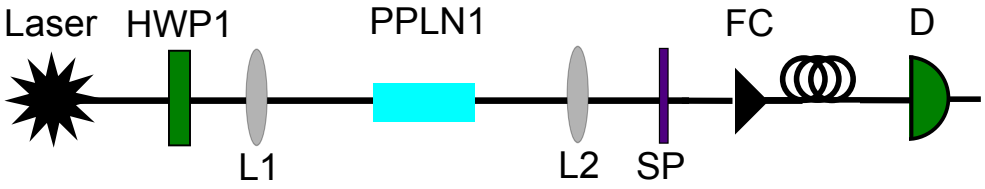

Figure 4.11: Setup for investigating intensity dependence on 532 nm SHG created from focusing a 0.5 mW of 1064 nm pump beam by a $f = 100$ mm lens (L1) into a PPLN crystal (PPLN1) and collimating with a $f = 100$ mm lens (L2). The pump beam is filtered with short-pass 720 nm filters (SP) before being fibre coupled (FC) and detected with a single-photon counter (D).

4.3.2 Power dependency

An important outcome of entanglement-enhanced ultrafast coincidence detection is the linear rate dependency with input power. In this case, we demonstrate that PPLN2, when pumped with a classical laser field, is quadratic in pump power. This is expected as SFG is dependent on the product of two electric fields (Fig. 2.1a), thus quadratic in intensity.

This power characterization was measured in a configuration similar to Fig. 4.11 with the results displayed in Fig. 4.12

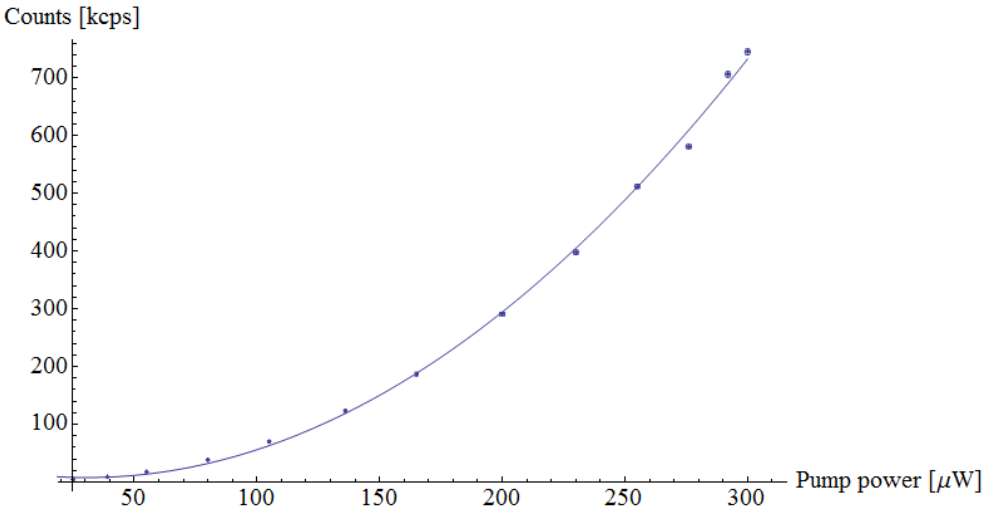

Figure 4.12: Quadratic intensity dependence of upconversion in PPLN taken at $T = 34.4°C$.

4.4 Experiment outlook

In summary to this chapter, a setup similar to O'Donnell and U'Ren [77] was designed and its major components characterized. Barring any further unexplained physical phenomena or effects related to either the source or the chosen components, I believe misalignment is the cause of the lack of upconverted signal.

Potential component upgrades include replacing the dispersive objectives with short focal length parabolic mirrors (dispersion-free) and building more robust resistive crystal heaters.

It would be beneficial to carry out further characterizations of the setup. In particular, it would be beneficial to analyze the behaviour of the prism compressor under a classical fs laser and autocorrelator.

In conclusion, the components of the experiment are operating in such a way that would suggest measurement of entanglement-enhanced coincidence detection in a nonlinear crystal is on the horizon.

Chapter 5

Conclusion

In this work, I demonstrated, in Chapter 2, the physics behind a cw SPDC source emitting spectrally broadband Type 0 downconversion temporally capable of ETPA. The spatial emission behaviour was found to be noncollinear. The opening half angle was measured experimentally on a beam profiler to be $(2.00 \pm 0.02)^\circ$, which compared well with the theoretically modelled half angle of 2.59°. To get a better understanding on the frequency-dependence of this conical emission, I experimentally measured the noncollinear emission from this source through a square notch filter of $\sigma = 10$ nm to have an experimental opening angle of $(1.84 \pm 0.02)^\circ$. This was comparable to the theoretical half opening angle of 1.47° which I modelled using a Gaussian notch filter of $\sigma = 10$ nm. In Chapter 4, I built an experimental setup theoretically capable of ultrafast coincidences of entangled photon pairs within a nonlinear crystal.

An obvious next step would be to demonstrate entanglement-enhanced ultrafast coincidence detection using this setup. After this, given the current experimental configuration, it would be fairly straightforward to replace the second nonlinear crystal with a highly two-photon absorbing medium, such as a laser dye like Rhodamine 6G. Theoretically, it would be beneficial to spectrally engineer a downconversion source which is further optimized temporally and spectrally for a specific fluorophore. In particular, it would be interesting to explore the feasibility of a SPDC source with positive frequency correlations to minimize relative signal-idler dispersion.

If the application of ETPA to microscopy is ultimately deemed impractical, there is still much to be gained and explored in the realm of ultrafast coincidences. Given the coherence ideas outlined in Chapter 3, it may be interesting to explore interesting applications of second-order interference via SLM phase manipulation. Furthermore, it would be beneficial to calculate the second-order correlation function for a given source of SPDC photons and

explore parameters to optimize this function, and subsequently, the ultrafast coincidence rate.

Outside of microscopy, it would be interesting to look at long interaction length ETPA for the purposes of quantum computing. Another interesting quantum optical direction could be to use ETPA to create subpoissonian states of light. In conclusion, this topic of ETPA has many interesting applications which push towards a greater understanding of physics.

Appendix A

Phasematching calculations

A.1 k surface

A clever way of visualizing the frequency-dependence of differing refractive indices is to examine the dispersion relation plotted in k_x, k_y, k_z space as a "k surface". The extraordinary solution is depicted as an ellipsoid of revolution, as seen in Fig. A.1, where the extraordinary solution is a sphere of radius $n_o k_o$. The k surface also gives an idea to the behaviour of the group velocity, or the first derivative.

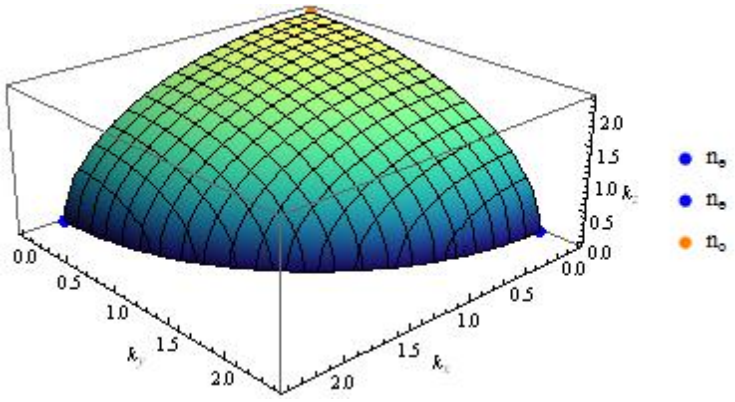

Figure A.1: "k-surface", or dispersion relation, of PPLN at $\lambda = 1064$ nm.

A.2 Integration tricks

A.2.1 Direct sinc function integration

When modelling intensities of SPDC, it is often necessary to integrate over modulus squared of the joint spectral density function. This often requires the tricky integration of the $\mathrm{sinc}^2(x)$. As soon as the argument of the sinc function becomes complicated, this integral is symbolically intractable.

The following integrals are useful in the situations where the arguement is of the form $b(x - x_0)$ or $a(x - x_0)^2$. Unfortunately, for the case of a Taylor expansion, this is not directly relevant.

$$\int_{-\infty}^{\infty} \mathrm{sinc}^2[b(x - x_0)]dx = \frac{\pi}{b} \tag{A.1}$$

$$\int_{-\infty}^{\infty} \mathrm{sinc}^2[a(x - x_0)^2]dx = \frac{1}{\sqrt{|a|}} \frac{4\sqrt{\pi}}{3} \tag{A.2}$$

A.3 Literature resources for modelling PPLN

The temperature-dependent Sellmeier equations used in this work are from Gayer *et al.* [85]. The ordinary and extraordinary refractive indices were used for 5% MgO-doped CLN. Another resource for $n_e(\lambda, T)$ is Jundt [88].

While I was searching for the above Sellmeier equations, I stumbled across the work of Paul *et al.* [83]. Here, the temperature-dependent poling period $\Lambda(T)$ was obtained. Note: this is for wavelengths in the range of 1.3-5 μm. Some inaccuracies in the simulation may be attributed to this.

A temperature-dependent PPLN crystal length function was also found in Jundt [88].

Appendix B

Iterations of the experimental setup

Here is both a chronological and pictorial journey of my Masters degree.

B.1 Waterloo, Fall 2011

After a month or so learning the fibre coupling basics under the guidance of another PhD student, I chose and purchased equipment and started building my first source.

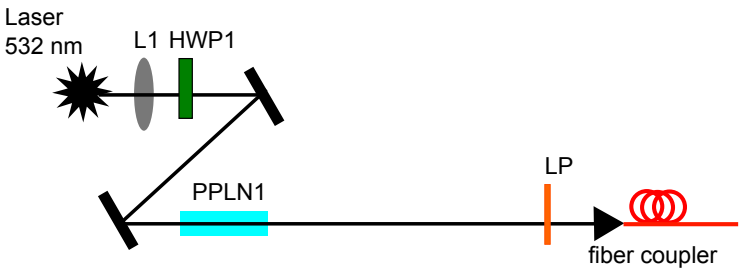

(a) Diagram

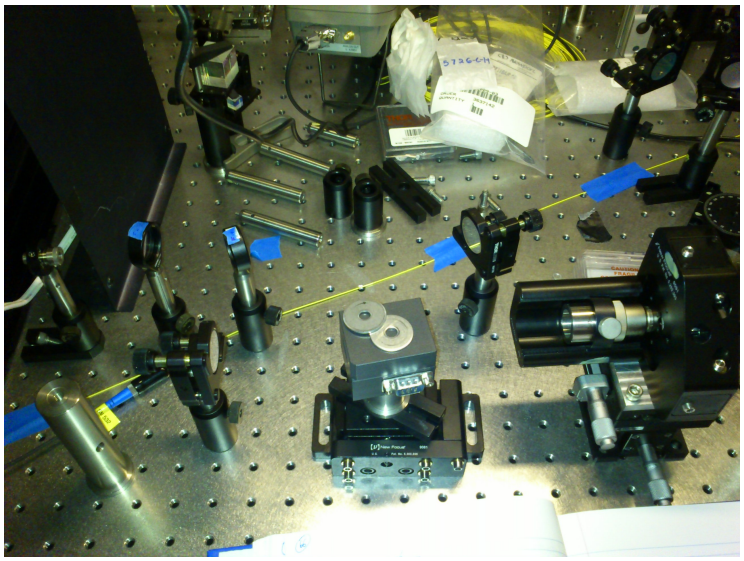

(b) Photograph

Figure B.1: Setup #1, built in Waterloo. A design for a downconversion source made with a $f = 22.5$ cm lens (L1) focusing the 532 nm beam into a 25 mm PPLN crystal (PPLN1) before the pump is filtered by a 776 nm long pass filter (LP). The downconversion would be focused via a $f = 15.6\ mm$ lens into multimode fiber within the fibercoupler (FC).

B.2 Vienna, January 2012

In January 2012, I flew to Vienna, Austria to work in the lab of Dr. Alipasha Vaziri with Dr. Robert Prevedel. Here, I properly characterized this downconversion source and briefly started work with diffraction gratings for dispersion cancellation.

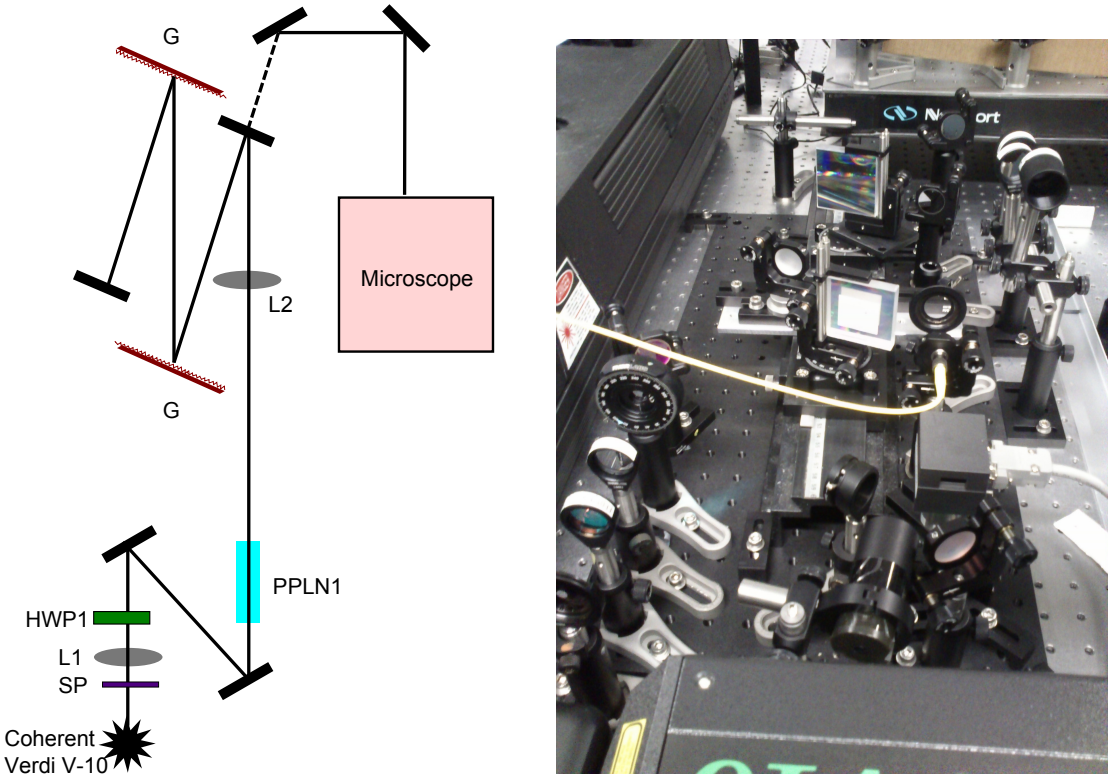

(a) Diagram

(b) Photograph

Figure B.2: Setup #2, built in Vienna. A design for a downconversion source made with a $f = 22.5$ cm lens (L1) focusing the 532 nm beam into a 25 mm PPLN crystal (PPLN1) before entering a grating compressor (G). A 776 nm longpass filter was used within the microscope to block the downconversion after the sample.

B.3 Waterloo, Winter-Spring 2012

Once I returned to Waterloo, I then set out to understand pulse compression and design both a grating and prism compressor for the ETPA application. At this time, two shorter, 5 mm PPLN crystals were obtained in order to reduce acquired GDD. At this time, most of the initial temperature-dependence characterizations were done on these short crystals.

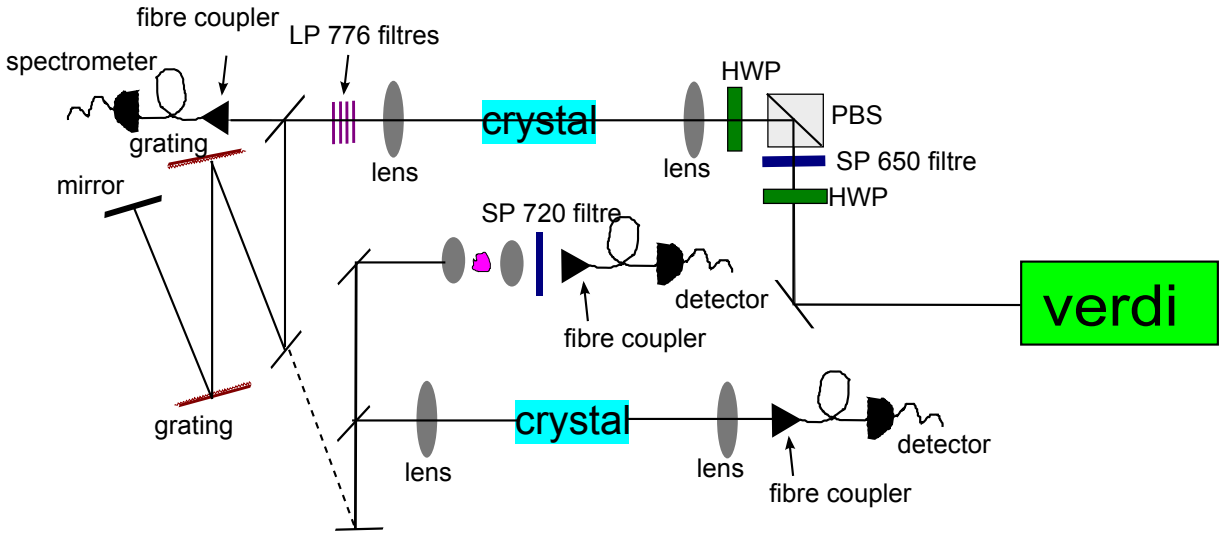

Figure B.3: Setup #3, built in Waterloo. Here, the polarization of a 532 nm Coherent Verdi beam is rotated appropriately to reflect off the polarizing beam splitter (PBS) and focused with a lens into the PPLN crystal at a vertical polarization. After filtering out the pump beam with four longpass filters, the downconversion enters into a grating compressor. The subsequent downconversion is focused into either a sample or a second PPLN crystal.

B.4 Vienna, Fall 2012

I returned to Vienna for a 3 month research trip, at the end of September 2012. Here, the grating experiment was fully realized.

Here, also, I took advantage of a 1064 nm, 30 fs pulsed laser to start a first version of a quadruple-pass prism compressor.

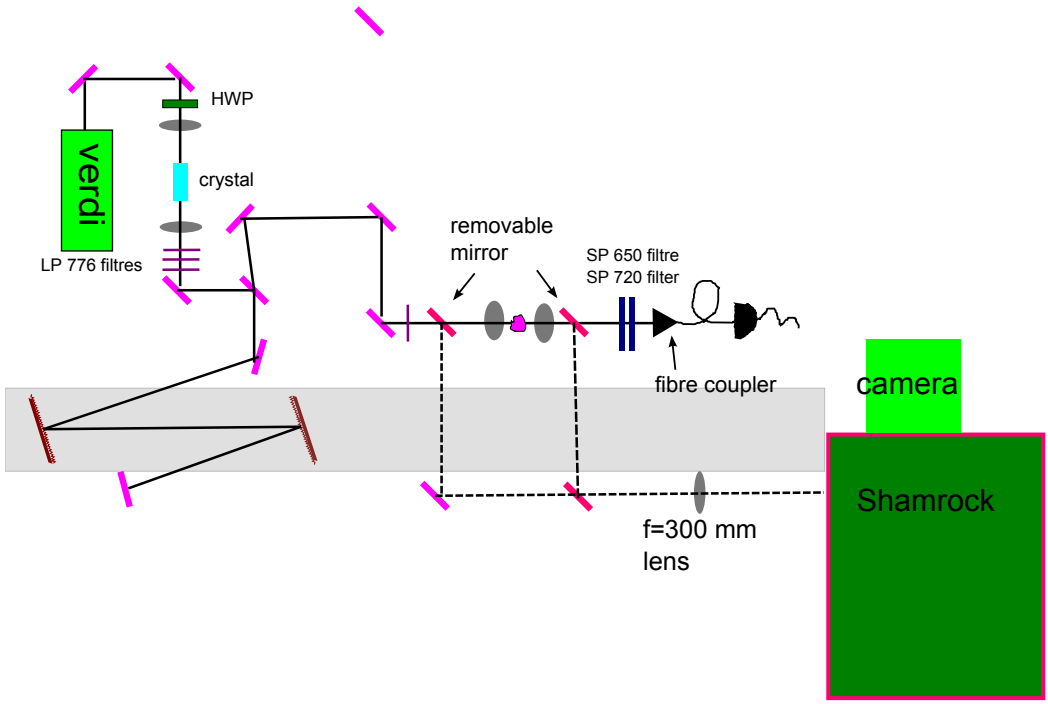

(a) Experiment diagram

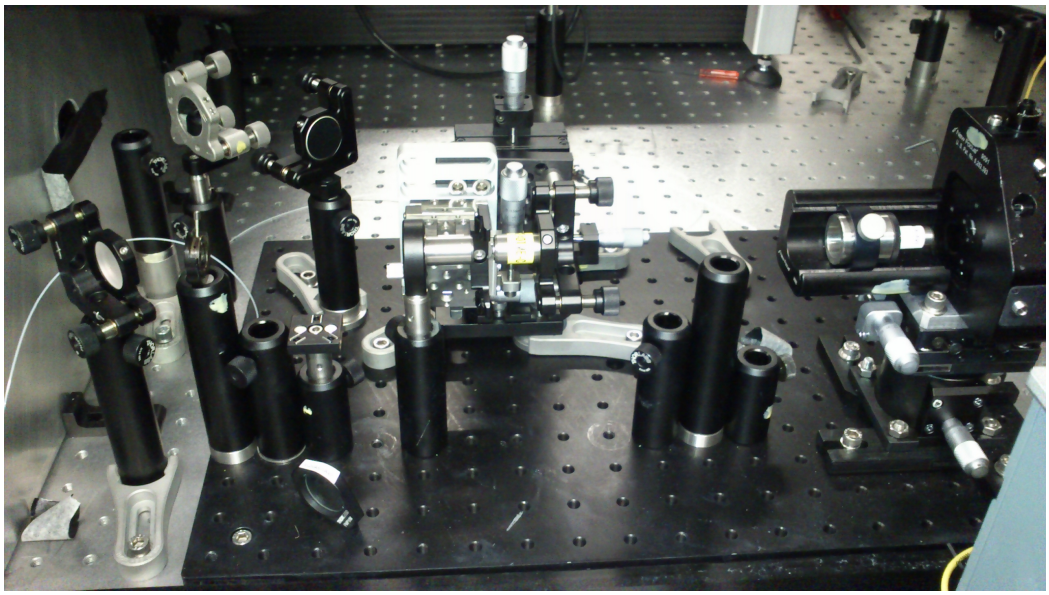

(b) Photograph of the imaging section of the apparatus.

Figure B.4: Setup #4, built in Vienna with to use with a emCCD camera/spectrometer system (Shamrock).

B.5 Waterloo, Winter-Spring 2013

Upon return to Waterloo, two different iterations of the setup were build. Setup #5 was rebuilt in an attempt for greater stability and accessibility (!).

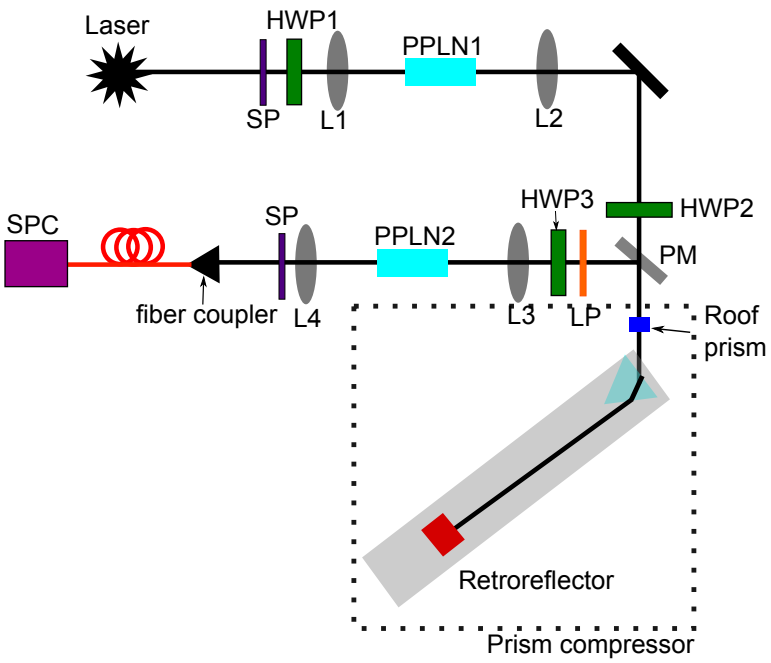

(a) Experiment diagram

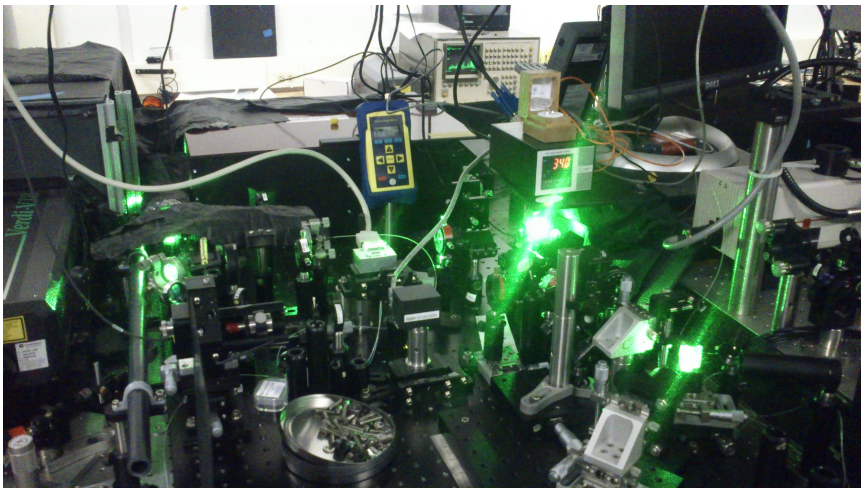

(b) Photograph of the imaging section of the apparatus.

Figure B.5: Setup #5, built in Waterloo with the quadruple-pass prism compressor.

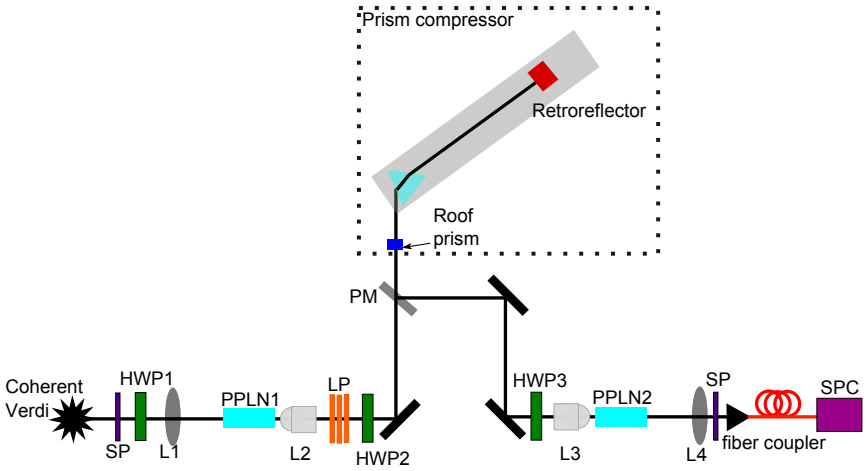

(a) Experiment diagram

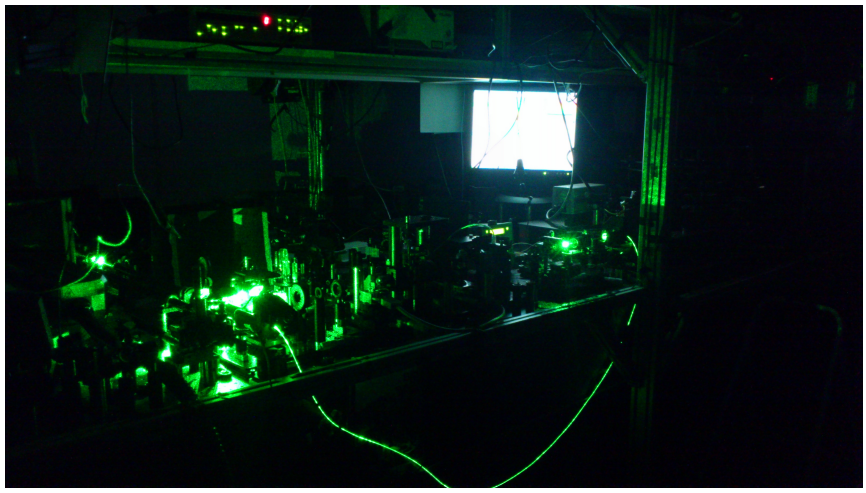

(b) Photograph of the imaging section of the apparatus.

Figure B.6: Setup #6, built in Waterloo with the quadruple-pass prism compressor. Photon pairs, centred around 1064 nm are created from focusing a $f = 100$ mm lens (L1) into a PPLN crystal (PPLN1) and collimating with an Olympus PLN 10x object (L2). The 1 W of 532 nm pump is filtered with long-pass 776 nm filters (LP). The polarization is rotated to horizontal by HWP2 before passing through a quadruple-pass prism compressor and being picked off by overhanging pick-off mirror (PM). The polarization is rotated back to vertical by HWP3 before the reverse process is then traversed where the SPDC pairs are focused, using L3, into PPLN2 and collimated, using L4=L1. A shortpass 720 nm filter (SP) is used to allow only the upconverted signal to pass.

Appendix C

Advice

A sarcastic guide to Masters-level graduate studies and research abroad.

C.1 Travel

Don't.

C.1.1 Visa applications

But if you must travel to Europe, keep your research tenure under the maximum visitor-allowed days in order to avoid needing a visa. Also, don't get paid, it also reduces the need for a visa. However, if you must apply for a visa, common sense dictates you apply many many many months in advance.

Visiting an embassy

When travelling to a different city to visit said embassy, always be sure your expected visiting date is not a national holiday of the other country.

Always have all documents with you when submitting a visa application, including the invisible, unmentioned documents. In the likely case you forgot said invisible, unmentioned documents, take no fear, they'll just stamp it and allow you to mail it in when you get home.

Tips for mailing a visa

Since you're most-likely tight on time, send the complete application express post. These fancy envelopes have the technology which allows you to retain a carbon copy receipt of your postage. Keep it.

Pay very close attention to the "To" and "From" box locations.

Track the mailed visa document often. After all, your passport is in it.

Finally, in any situation, time-pressured or not, never mail important documents to yourself.

C.1.2 How not to fly internationally

Never completely fill your waterbottle after passing through security. There will always be a surprise extra security checkpoint to pass through which will require regulation amount of liquids on your person (read: none). Under the likely situation where you forget this information, you will need to guzzle 1 L of water very quickly, which will result in large amounts of spillage down the front of your shirt. Given that you probably haven't showered in many hours, this may not be a bad thing.

How to lose your luggage

Always, always, always pack the following in your carry-on:

- a change of clothes
- toothbrush
- electronic chargers

because you WILL lose your luggage. It is also useful to know the brand name of your luggage when approaching the lost luggage desk.

C.1.3 Living in a foreign country

Finding accommodations

Try to avoid apartment fraud.

Work-life balance is important. As convenient as living down the hall from the lab is, try to breathe fresh air at least twice a day by having an apartment in another building.

C.1.4 Research abroad

The number one rule of experimental research abroad is that the equipment you need is always in the other lab, on the other side of the ocean. The second rule, regardless of how hard you try, all imperial and metric parts will inevitably become mixed together.

Keep a good lab book. Take pictures of different iterations of your experiment, it may come in handy (see Appendix B). Do the best science you can. The "mute" button on group meeting Skype calls is also incredibly useful.

Shipping parts

- metric vs imperial - the never-ending challenge!
- It never arrives in time

  your precious research time is a-wasting!

A wise postdoc once recommended to pay for an extra piece of luggage and keep your experiment on your person. Problems with that:

- Customs can be scary
- You should have strength enough to deadlift all your packed bags up steep steps of a train before it departs

References

[1] J. D. Franson, B. C. Jacobs, and T. B. Pittman. Quantum computing using single photons and the Zeno effect. *Phys. Rev. A*, 70:062302, Dec 2004.

[2] G. Brida, M. Genovese, and I. R. Berchera. Experimental realization of sub-shot-noise quantum imaging. *Nat. Photon.*, 4(12):227–230, April 2010.

[3] M. Göppert-Mayer. Über elementarakte mit zwei quantensprüngen. *Ann. Phys.*, 401(3):273–294, 1931.

[4] R. W. Boyd. *Nonlinear optics*. Academic Press, Amsterdam, third edition, 2008.

[5] W. Kaiser and C. G. B. Garrett. Two-photon excitation in $CaF_2 : Eu^{2+}$. *Phys. Rev. Lett.*, 7:229–231, Sep 1961.

[6] T. H. Maiman. Stimulated optical radiation in ruby. *Nature*, 187(4736):493–494, 1960.

[7] M. Pawlicki, H. A. Collins, R. G. Denning, and H. L. Anderson. Two-photon absorption and the design of two-photon dyes. *Angew. Chem. (Int. ed.)*, 48(18):3244–3266, 2009.

[8] W. Denk, J. H. Strickler, and W. W. Webb. Two-photon laser scanning fluorescence microscopy. *Science*, 248(4951):73–76, 1990.

[9] W. Denk. Two-photon excitation in functional biological imaging. *J. Biomed. Opt.*, 1(3):296–304, 1996.

[10] F. Helmchen and W. Denk. Deep tissue two-photon microscopy. *Nat. Meth.*, 2(12):932–940, 2005.

[11] E. E. Hoover and J. A. Squier. Advances in multiphoton microscopy technology. *Nat. Photon.*, 7:93–101, 2013.

[12] W. Denk, D. W. Piston, and W. W. Webb. Multi-photon molecular excitation in laser-scanning microscopy. In James B. Pawley, editor, *Handbook of Biological Confocal Microscopy*, chapter 28, pages 535–549. Springer, New York, 3 edition, 2006.

[13] C. Xu and W. W. Webb. Measurement of two-photon excitation cross sections of molecular fluorophores with data from 690 to 1050 nm. *J. Opt. Soc. Am. B*, 13(3):481–491, Mar 1996.

[14] J.-C. Diels and W. Rudolph. *Ultrashort laser pulse phenomena: fundamentals, techniques, and applications on a femtosecond time scale*. Academic Press, Boston, second edition, 2006.

[15] B. E. A. Saleh and M. C. Teich. *Fundamentals of Photonics*. Wiley-Interscience, Hoboken, 2nd ed edition, 2007.

[16] M. Müller, J. Squier, R. Wolleschensky, U. Simon, and G. J. Brakenhoff. Dispersion pre-compensation of 15 femtosecond optical pulses for high-numerical-aperture objectives. *J. Microscopy*, 191(2):141–150, 1998.

[17] U. Keller. Ultrafast solid-state lasers. volume 46 of *Progress in Optics*, pages 1 – 115. Elsevier, 2004.

[18] E. Miesak and R. Negres. Alignment procedure for a dual grating pulse compressor. *Appl. Opt.*, 37(34):8146–8147, Dec 1998.

[19] J. Javanainen and P. L. Gould. Linear intensity dependence of a two-photon transition rate. *Phys. Rev. A*, 41:5088–5091, May 1990.

[20] J. Gea-Banacloche. Two-photon absorption of nonclassical light. *Phys. Rev. Lett.*, 62:1603–1606, Apr 1989.

[21] N. Ph. Georgiades, E. S. Polzik, K. Edamatsu, H. J. Kimble, and A. S. Parkins. Nonclassical excitation for atoms in a squeezed vacuum. *Phys. Rev. Lett.*, 75:3426–3429, Nov 1995.

[22] B. Dayan. Theory of two-photon interactions with broadband down-converted light and entangled photons. *Phys. Rev. A*, 76:043813, Oct 2007.

[23] B. Dayan, A. Pe'er, A. A. Friesem, and Y. Silberberg. Nonlinear interactions with an ultrahigh flux of broadband entangled photons. *Phys. Rev. Lett.*, 94:043602, Feb 2005.

[24] D. Meshulach and Y. Silberberg. Coherent quantum control of two-photon transitions by a femtosecond laser pulse. *Nature*, 396(3):239–242, November 1998.

[25] Z. Zheng and A. M. Weiner. Spectral phase correlation of coded femtosecond pulses by second-harmonic generation in thick nonlinear crystals. *Opt. Lett.*, 25(13):984–986, Jul 2000.

[26] Z. Zheng and A.M. Weiner. Coherent control of second harmonic generation using spectrally phase coded femtosecond waveforms. *Chem. Phys.*, 267(1-3):161–171, 2001.

[27] B. Dayan, A. Pe'er, A.A. Friesem, and Y. Silberberg. Coherent control with broadband squeezed vacuum. *arXiv preprint quant-ph/*, 2003. 0302038v1.

[28] M. C. Teich and B. E. A. Saleh. Entangled-photon microscopy. *Cesk. Cas. Fyz*, 8:3–8, 1997.

[29] M. C. Teich and B. E. A. Saleh. Entangled-photon microscopy, spectroscopy, and display. U.S. Patent No. 5796477, August 1998.

[30] K. König, P. T. C. So, W. W. Mantulin, and E. Gratton. Cellular response to near-infrared femtosecond laser pulses in two-photon microscopes. *Opt. Lett.*, 22(2):135–136, Jan 1997.

[31] C. A. Kocher and E. D. Commins. Polarization correlation of photons emitted in an atomic cascade. *Phys. Rev. Lett.*, 18:575–577, Apr 1967.

[32] S. J. Freedman and J. F. Clauser. Experimental test of local hidden-variable theories. *Phys. Rev. Lett.*, 28:938–941, Apr 1972.

[33] P. Michler, A. Imamoglu, M. D. Mason, P. J. Carson, G. F. Strouse, and S. K. Buratto. Quantum correlation among photons from a single quantum dot at room temperature. *Nature*, 406(6799):968–970, aug 2000.

[34] C. Santori, M. Pelton, G. Solomon, Y. Dale, and Y. Yamamoto. Triggered single photons from a quantum dot. *Phys. Rev. Lett.*, 86:1502–1505, Feb 2001.

[35] O. Benson, C. Santori, M. Pelton, and Y. Yamamoto. Regulated and entangled photons from a single quantum dot. *Phys. Rev. Lett.*, 84:2513–2516, Mar 2000.

[36] H. Takesue and K. Inoue. Generation of polarization-entangled photon pairs and violation of Bell's inequality using spontaneous four-wave mixing in a fiber loop. *Phys. Rev. A*, 70:031802, Sep 2004.

[37] H. Takesue and K. Inoue. Generation of 1.5-μm band time-bin entanglement using spontaneous fiber four-wave mixing and planar light-wave circuit interferometers. *Phys. Rev. A*, 72:041804, Oct 2005.

[38] Z. Y. Ou and L. Mandel. Violation of Bell's inequality and classical probability in a two-photon correlation experiment. *Phys. Rev. Lett.*, 61:50–53, Jul 1988.

[39] Y. H. Shih and C. O. Alley. New type of Einstein-Podolsky-Rosen-Bohm experiment using pairs of light quanta produced by optical parametric down conversion. *Phys. Rev. Lett.*, 61:2921–2924, Dec 1988.

[40] J. Brendel, N. Gisin, W. Tittel, and H. Zbinden. Pulsed energy-time entangled twin-photon source for quantum communication. *Phys. Rev. Lett.*, 82:2594–2597, Mar 1999.

[41] J. G. Rarity and P. R. Tapster. Two-color photons and nonlocality in fourth-order interference. *Phys. Rev. A*, 41:5139–5146, May 1990.

[42] A. Mair, A. Vaziri, G. Weihs, and A. Zeilinger. Entanglement of the orbital angular momentum states of photons. *Nature*, 412(6844):313–316, July 2001.

[43] Z. Y. Ou, X. Y. Zou, L. J. Wang, and L. Mandel. Observation of nonlocal interference in separated photon channels. *Phys. Rev. Lett.*, 65:321–324, Jul 1990.

[44] J. G. Rarity, P. R. Tapster, E. Jakeman, T. Larchuk, R. A. Campos, M. C. Teich, and B. E. A. Saleh. Two-photon interference in a Mach-Zehnder interferometer. *Phys. Rev. Lett.*, 65:1348–1351, Sep 1990.

[45] J. T. Barreiro, N. K. Langford, N. A. Peters, and P. G. Kwiat. Generation of hyperentangled photon pairs. *Phys. Rev. Lett.*, 95:260501, Dec 2005.

[46] M. H. Rubin, D. N. Klyshko, Y. H. Shih, and A. V. Sergienko. Theory of two-photon entanglement in type-II optical parametric down-conversion. *Phys. Rev. A*, 50:5122–5133, Dec 1994.

[47] Z. Y. Ou, L. J. Wang, and L. Mandel. Vacuum effects on interference in two-photon down conversion. *Phys. Rev. A*, 40:1428–1435, Aug 1989.

[48] R. Ghosh, C. K. Hong, Z. Y. Ou, and L. Mandel. Interference of two photons in parametric down conversion. *Phys. Rev. A*, 34:3962–3968, Nov 1986.

[49] D. S. Hum and M. M. Fejer. Quasi-phasematching. *Comptes Rendus Physique*, 8(2):180 – 198, 2007. Recent advances in crystal optics.

[50] N. Boeuf, D. Branning, I. Chaperot, E. Dauler, S. Guérin, G. Jaeger, A. Muller, and A. Migdall. Calculating characteristics of noncollinear phase matching in uniaxial and biaxial crystals. *Opt. Eng.*, 39(4):1016–1024, 2000.

[51] J. A. Armstrong, N. Bloembergen, J. Ducuing, and P. S. Pershan. Interactions between light waves in a nonlinear dielectric. *Phys. Rev.*, 127:1918–1939, Sep 1962.

[52] M. Yamada, N. Nada, M. Saitoh, and K. Watanabe. First–order quasi–phase matched $LiNbO_3$ waveguide periodically poled by applying an external field for efficient blue second–harmonic generation. *Applied Physics Letters*, 62(5), 1993.

[53] R. L. Byer. Quasi-phasematched nonlinear interactions and devices. *J. Nonlinear Opt. Phys. & Mat.*, 06(04):549–592, 1997.

[54] P. Kolenderski, W. Wasilewski, and K. Banaszek. Modeling and optimization of photon pair sources based on spontaneous parametric down-conversion. *Phys. Rev. A*, 80:013811, Jul 2009.

[55] S.-Y. Baek and Y.-H. Kim. Spectral properties of entangled photons generated via Type-I frequency-nondegenerate spontaneous parametric down-conversion. *Phys. Rev. A*, 80:033814, Sep 2009.

[56] S.P. Walborn, C.H. Monken, S. Pádua, and P.H. Souto Ribeiro. Spatial correlations in parametric down-conversion. *Physics Reports*, 495(4-5):87 – 139, 2010.

[57] A. Fedrizzi, T. Herbst, A. Poppe, T. Jennewein, and A. Zeilinger. A wavelength-tunable fiber-coupled source of narrowband entangled photons. *Opt. Express*, 15(23):15377–15386, Nov 2007.

[58] DataRay Inc., 14505 Seaman Gulch Road, Bella Vista, CA 96008, USA. *WinCamD Series Laser Beam Images User Manual*.

[59] R. J. Glauber. The quantum theory of optical coherence. *Phys. Rev.*, 130:2529–2539, Jun 1963.

[60] P. W. Milonni and J. H. Eberly. *Laser Physics*. John Wiley & Sons, Hoboken, 2010.

[61] C. Gerry and P. Knight. *Introduction to Quantum Optics*. Cambridge University Press, New York, 2004.

[62] M. D. Eisaman, J. Fan, A. Migdall, and S. V. Polyakov. Invited review article: Single-photon sources and detectors. *Rev. Sci. Instr.*, 82(7):071101, July 2011.

[63] L. Mandel and E. Wolf. *Optical coherence and quantum optics*. Cambridge University Press, New York, 1995.

[64] Z. Y. Ou. Quantum theory of fourth-order interference. *Phys. Rev. A*, 37:1607–1619, Mar 1988.

[65] R. Loudon. *The Quantum Theory of light*. Oxford University Press, Oxford, third edition, 2010.

[66] R. J. Glauber. *Quantum theory of optical coherence: selected papers and lectures*. Wiley-VCH, Weinheim, 2007.

[67] R. Hanbury Brown and R. Q. Twiss. Correlation between photons in two coherent beams of light. *Nature*, 177(4497):27–29, 1956.

[68] V. Torres-Company, A. Valencia, M. Hendrych, and J. P. Torres. Cancellation of dispersion and temporal modulation with nonentangled frequency-correlated photons. *Phys. Rev. A*, 83:023824, Feb 2011.

[69] F. Boitier, A. Godard, N. Dubreuil, P. Delaye, C. Fabre, and E. Rosencher. Two-photon-counting interferometry. *Phys. Rev. A*, 87:013844, Jan 2013.

[70] B. R. Mollow. Two-photon absorption and field correlation functions. *Phys. Rev.*, 175:1555–1563, Nov 1968.

[71] G. S. Agarwal. Field-correlation effects in multiphoton absorption processes. *Phys. Rev. A*, 1:1445–1459, May 1970.

[72] F. Boitier, A. Godard, E. Rosencher, and C. Fabre. Measuring photon bunching at ultrashort timescale by two-photon absorption in semiconductors. *Nat. Phys.*, 5(4):267–270, March 2009.

[73] A. Joobeur, B. E. A. Saleh, and M. C. Teich. Spatiotemporal coherence properties of entangled light beams generated by parametric down-conversion. *Phys. Rev. A*, 50:3349–3361, Oct 1994.

[74] D. C. Burnham and D. L. Weinberg. Observation of simultaneity in parametric production of optical photon pairs. *Phys. Rev. Lett.*, 25:84–87, Jul 1970.

[75] T. E. Keller and M. H. Rubin. Theory of two-photon entanglement for spontaneous parametric down-conversion driven by a narrow pump pulse. *Phys. Rev. A*, 56:1534–1541, Aug 1997.

[76] B. R. Mollow. Photon correlations in the parametric frequency splitting of light. *Phys. Rev. A*, 8:2684–2694, Nov 1973.

[77] K. A. O'Donnell and A. B. U'Ren. Time-resolved up-conversion of entangled photon pairs. *Phys. Rev. Lett.*, 103:123602, Sep 2009.

[78] B. Dayan, A. Pe'er, A. A. Friesem, and Y. Silberberg. Two photon absorption and coherent control with broadband down-converted light. *Phys. Rev. Lett.*, 93:023005, Jul 2004.

[79] R. Ghosh, C. K. Hong, Z. Y. Ou, and L. Mandel. Interference of two photons in parametric down conversion. *Phys. Rev. A*, 34:3962–3968, Nov 1986.

[80] M. Bellini, F. Marin, S. Viciani, A. Zavatta, and F. T. Arecchi. Nonlocal pulse shaping with entangled photon pairs. *Phys. Rev. Lett.*, 90:043602, Jan 2003.

[81] A. Pe'er, B. Dayan, A. A. Friesem, and Y. Silberberg. Temporal shaping of entangled photons. *Phys. Rev. Lett.*, 94:073601, Feb 2005.

[82] C. Bernhard, B. Bessire, T. Feurer, and A. Stefanov. Shaping frequency-entangled qudits. *Phys. Rev. A*, 88:032322, Sep 2013.

[83] O. Paul, A. Quosig, T. Bauer, M. Nittmann, J. Bartschke, G. Anstett, and J.A. L'Huillier. Temperature-dependent Sellmeier equation in the MIR for the extraordinary refractive index of 5% MgO doped congruent $LiNbO_3$. *Appl. Phys. B*, 86(1):111–115, 2007.

[84] J. B. Guild, C. Xu, and W. W. Webb. Measurement of group delay dispersion of high numerical aperture objective lenses using two-photon excited fluorescence. *Applied Optics*, 36(1):397–401, jan 1997.

[85] O. Gayer, Z. Sacks, E. Galun, and A. Arie. Temperature and wavelength dependent refractive index equations for MgO-doped congruent and stoichiometric $LiNbO_3$. *Appl. Phys. B*, 91(2):343–348, 2008.

[86] R. L. Fork, O. E. Martinez, and J. P. Gordon. Negative dispersion using pairs of prisms. *Opt. Lett.*, 9(5):150–152, May 1984.

[87] S. Akturk, X. Gu, M. Kimmel, and R. Trebino. Extremely simple single-prism ultrashort- pulse compressor. *Opt. Express*, 14(21):10101–10108, Oct 2006.

[88] D. H. Jundt. Temperature-dependent Sellmeier equation for the index of refraction, n_e, in congruent lithium niobate. *Opt. Lett.*, 22(20):1553–1555, Oct 1997.